

# Nonlocal Willis Dynamic Homogenization Theory for Active Metabeams

Shaoyun Wang

*Department of Mechanical and Aerospace Engineering, University of Missouri, Columbia, Missouri 65211, USA*

Guoliang Huang\*

*Department of Mechanics and Engineering Science, College of Engineering, Peking University, Beijing 100871, PR China*

---

## Abstract

Unlike classical elasticity, Willis media exhibit coupling between stress–velocity and momentum–strain, capturing additional dynamic interactions in heterogeneous systems. While previous studies have predominantly focused on the homogenization of passive Willis media, extending these concepts to active systems remains largely unexplored. In this work, we employ a nonlocal Willis dynamic homogenization for active metabeams that integrates sensor–actuator pairs into a background beam to induce nonreciprocal coupling. By employing a source-driven homogenization approach, our EMT accurately captures the full dispersion curves over the entire Brillouin zone—overcoming the limitations of static or long-wavelength theories—and enables the definition of a winding number for the frequency spectrum under periodic boundary conditions (PBC). **imaginary part, continuum media** Notably, our framework predicts the emergence of low-frequency shear waves, absent in traditional beam theory, and facilitates direction-dependent wave amplification and attenuation. Through asymptotic analysis, we determine the frequency spectrum under open boundary conditions (OBC) and reveal its relationship to the periodic spectrum, with the resulting eigenmodes (skin modes) exhibiting pronounced edge localization that can be characterized by the generalized Brillouin zone (GBZ). Furthermore, we establish a bulk–boundary correspondence (BBC) that links the winding number to the localization direction of skin modes, providing a practical alternative to directly computing the GBZ. Finally, we demonstrate applications in nonreciprocal filtering, amplification, and interface-localized energy harvesting, paving the way for next-generation active mechanical metamaterials with tailored wave functionalities.

**Keywords:** Willis medium, dynamic homogenization, non-Hermiticity, nonlocality, nonreciprocity, topology

---

## 1. Introduction

Momentum, a conserved quantity proportional to the product of density and velocity, arises as a consequence of spatial homogeneity according to Noether’s theorem (Landau et al., 1976; Goldstein et al., 2002). In contrast, the stress-strain relation—stating that stress is proportional to an elastic constant times strain—is an empirical law characterizing specific material behavior (Landau et al., 1986). Despite their differing physical origins, momentum–velocity and stress-strain pairs share a fundamental similarity: they both act as conjugate variables in the Lagrangian formalism. Classical elasticity treats them independently, but Willis media introduce cross-

---

\*Corresponding author

Email address: guohuang@pku.edu.cn (Guoliang Huang)

8 couplings—termed Willis couplings—between momentum and strain, as well as stress and velocity, modifying con-  
9 ventional elastic behavior (Willis, 1981, 1997). These couplings necessitate new homogenization methods including  
10 Green’s function methods and field averaging (Willis, 2009, 2011, 2012; Milton and Willis, 2010; Nemat-Nasser and  
11 Srivastava, 2011; Shuvalov et al., 2011; Norris et al., 2012; Srivastava, 2015; Nassar et al., 2015), asymptotic ho-  
12 mogenization (Nassar et al., 2016), perturbative expansions combined with field averaging (Qu et al., 2022; Milton,  
13 2007), and mode expansion with subspace projection (Ponge et al., 2017; Pernas-Salomón and Shmuel, 2018). Such  
14 approaches have extended Willis couplings to acoustics (Muhlestein et al., 2017; Li et al., 2022, 2024) and piezoelec-  
15 tricity (Pernas-Salomón and Shmuel, 2020b; Pernas-Salomón et al., 2021; Pernas-Salomón and Shmuel, 2020a; Lee  
16 et al., 2023; Baz, 2024; Muñafra et al., 2023). However, homogenization in active systems, where artificial couplings  
17 arise, remains challenging. Source-driven homogenization (Sieck et al., 2017) offers a systematic framework for incor-  
18 porating background media and scatterers, making it a promising approach for studying active systems. This study  
19 extends source-driven homogenization to a non-Hermitian Willis metabeam with sensor–actuator elements, breaking  
20 major symmetry (Fig. 1). We develop an effective medium model that captures high-frequency and short-wavelength  
21 wave behavior, advancing both theoretical and practical understanding of active Willis materials.

22 Willis media, derived from homogenization theory, exhibit unique properties that drive advanced metamaterial  
23 design. In cloaking, transformed media extend beyond classical elasticity and align with the Milton–Briane–Willis  
24 gauge (Milton et al., 2006; Chen and Haberman, 2023). Willis coupling enables asymmetric reflection (Liu et al., 2019;  
25 Muhlestein et al., 2017) and precise control over polarization, mode conversion, wavefront shaping, and independent  
26 reflection/transmission tuning (Qu et al., 2022; Chen et al., 2020; Li et al., 2018). While most studies focus on passive  
27 Willis systems, integrating active elements, particularly sensor–actuator pairs, leads to novel effects like direction-  
28 dependent wave amplification (Cheng and Hu, 2022) and nonreciprocal wave propagation (Zhai et al., 2019). Despite  
29 these advances, key aspects such as non-Hermiticity, topology (bulk–boundary correspondence), symmetry properties,  
30 and space–time duality remain largely unexplored (Christensen et al., 2024; Yves et al., 2024; Ashida et al., 2020;  
31 Galiffi et al., 2022).

32 In classical elasticity, material properties remain constant (Landau et al., 1986), whereas metamaterials exhibit  
33 frequency-dependent properties, enabling effects like bandgaps (Huang et al., 2009) and negative refraction (Zhu  
34 et al., 2014). Willis media extend this by introducing both temporal nonlocality (frequency dispersion) and spatial  
35 nonlocality (spatial dispersion). While spatial dispersion is well-established in optics—leading to anisotropic prop-  
36 agation, gyrotropy, and directed energy flow (Agranovich and Ginzburg, 2013; Shokri and Rukhadze, 2019)—it is  
37 uncommon in elasticity. In structured elastic media, it couples material properties to both frequency and wavenum-  
38 ber, altering wave interactions. For free waves, effective properties follow dispersion relations, but external loads that  
39 depend on both parameters can excite waves with arbitrary frequencies and wavenumbers. This nonlocality is cru-  
40 cial for capturing high-frequency and short-wavelength behavior, essential for understanding spectral topology under  
41 PBCs and skin modes under OBCs. However, it also complicates boundary value problems by requiring nonlocal  
42 boundary conditions.

43 Non-Hermitian systems have advanced significantly since Carl Bender’s discovery that PT-symmetric non-Hermitian  
44 operators can have entirely real eigenvalues (Bender and Boettcher, 1998), challenging the notion that Hermiticity is  
45 necessary for real spectra (Sakurai and Napolitano, 2017) and expanding research in non-Hermitian physics (Bender

and Hook, 2024). Varying non-Hermitian couplings induces PT-symmetry breaking, leading to a phase transition from real to complex eigenvalues (Ashida et al., 2020). At the transition point (exceptional point), eigenvalues and eigenvectors coalesce, enabling novel effects such as enhanced sensor sensitivity and unconventional laser modes (Miri and Alu, 2019). Simultaneously, the study of topological insulators, rooted in bulk-boundary correspondence, faces challenges in non-Hermitian systems due to the breakdown of Bloch band theory. This leads to non-Bloch band theory and the discovery of the non-Hermitian skin effect (Yao and Wang, 2018), which establishes a new form of bulk-boundary correspondence linking the winding number of the complex frequency spectrum under PBC to skin modes under OBC (Okuma et al., 2020; Zhang et al., 2020). Many quantum non-Hermitian findings extend naturally to classical wave systems, including electromagnetic and acoustic waves, due to their shared mathematical framework—eigenvalue problems in the Hilbert space. Non-Hermitian skin modes appear in elastic systems (Chen et al., 2021), interface modes in metaplates (Wang et al., 2024), and bulk-boundary correspondence in discrete systems (Wu et al., 2024). However, a systematic exploration of the frequency spectrum under both PBC and OBC, particularly the role of the GBZ in governing skin modes and extending bulk-boundary correspondence to nonlocal non-Hermitian Willis systems, remains an open question.

Elastic beams with piezoelectric patches and integrated circuitry serve as a versatile platform for studying unconventional elastic waves. They enable observations of the non-Hermitian skin effect (Chen et al., 2021), odd mass density (Wu et al., 2023), temporal reflection (Wang et al., 2025), frequency conversion (Wu et al., 2022), and topological pumping (Xia et al., 2021). Beam models also advance Willis media research, from dynamic homogenization of inhomogeneous Euler–Bernoulli beams (Pernas-Salomón and Shmuel, 2018) to parameter retrieval in Timoshenko beams with multiple scatterers (Liu et al., 2019; Chen et al., 2020). However, developing a complete EMT for active Timoshenko beams with multiple scatterers remains an open challenge.

Motivated by the microstructure design in Chen et al. (2020), we introduce non-Hermiticity into a background beam by embedding sensor–actuator pairs that generate nonreciprocal coupling. Employing a source-driven homogenization method, we develop an effective medium theory for nonlocal non-Hermitian Willis metabeam. This theory accurately reproduces the full dispersion curves over the entire Brillouin zone—overcoming the limitations of static or long-wavelength homogenization approaches—and enables the definition of a winding number for the spectrum under PBC. Moreover, our framework predicts the emergence of a low-frequency shear wave, absent in traditional beam theory, and facilitates nonreciprocal wave amplification and attenuation. Through asymptotic analysis, we calculate the frequency spectrum under OBC and reveal its relationship to the spectrum under PBC. The resulting eigenmodes, or skin modes, under OBC exhibit pronounced edge localization, whose extent can be characterized by the GBZ derived from the asymptotic analysis. Furthermore, we establish a rigorous bulk–boundary correspondence for nonlocal non-Hermitian Willis media, elucidating the interplay between the winding number and skin modes; this correspondence allows one to determine the localization direction of the skin modes using the winding number rather than the computationally challenging GBZ. Finally, we demonstrate practical applications—including nonreciprocal filters and amplifiers and interface-localized energy harvesting—paving the way for the next generation of active mechanical metamaterials with tailored wave functionalities.

This paper is organized as follows. Section 2 presents the source-driven homogenization approach for nonlocal non-Hermitian Willis metabeam with embedded sensor-actuator elements. Section 3 validates the proposed EMT

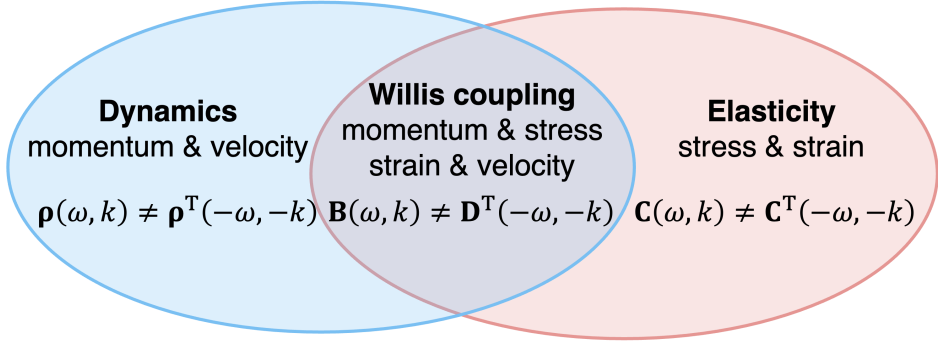


Figure 1: Possible constitutive operators in elastodynamics with broken major symmetry. The broken major symmetry of the elastic tensor  $\mathbf{C}(\omega, k) \neq \mathbf{C}^T(-\omega, -k)$ , density tensor  $\rho(\omega, k) \neq \rho^T(-\omega, -k)$ , and Willis coupling tensor  $\mathbf{B}(\omega, k) \neq \mathbf{D}^T(-\omega, -k)$  leads to the non-Hermitian media.

by comparing theoretical dispersion predictions with COMSOL simulations across various parameter regimes. Section 4 analyzes key wave phenomena, including low-frequency shear waves, nonreciprocal wave amplification and attenuation, asymptotic analysis of the open-boundary spectrum, and bulk–boundary correspondence. Section 5 explores practical applications such as nonreciprocal filtering, amplification, and interface-localized energy harvesting. Finally, Section 6 summarizes the main findings and outlines future research directions. Additional derivations and supporting materials are provided in the Appendices.

## 2. Effective medium theory of nonlocal non-Hermitian Willis metabeam

In this section, we apply EMT to derive the effective constitutive relations for a metabeam embedded with sensor-actuators (Fig. 2(a)). The homogenization process is illustrated in Fig. 2(b), where sensors and actuators are modeled as embedded scatterers. We first introduce the Timoshenko beam equations (Section 2.1), forming the theoretical foundation. The background beam response under external sources (Fig. 2(b), top panel) is analyzed in Section 2.2, followed by the effective medium response (Fig. 2(b), bottom panel) in Section 2.3. The total response (Fig. 2(b), middle panel), comprising the microscale local response (Section 2.4) and mesoscale multiple scattering effects (Section 2.5), leads to the derivation of the effective constitutive relations (Section 2.6). Finally, we formulate the nonlocal governing equations and boundary value problem (BVP) in Section 2.7.

### 2.1. Fundamental Equations of the Timoshenko Beam

Consider a Timoshenko beam characterized by mass density  $\rho$ , Young's modulus  $E$ , and shear modulus  $G$ . The material's response is governed by the balance of linear momentum  $\mu$  and angular momentum  $J$  (Yao et al., 2009; Chen et al., 2020)

$$\begin{aligned}\partial_t \mu &= \partial_x F + f, \\ \partial_t J &= \partial_x M + F + q,\end{aligned}\tag{1}$$

where  $F$  denotes the shear force,  $M$  represents the bending moment, and  $f$  and  $q$  correspond to the external body torque and transverse body force, respectively. The bending curvature  $\kappa$ , shear strain  $\gamma$ , rotational angle  $\psi$ , and

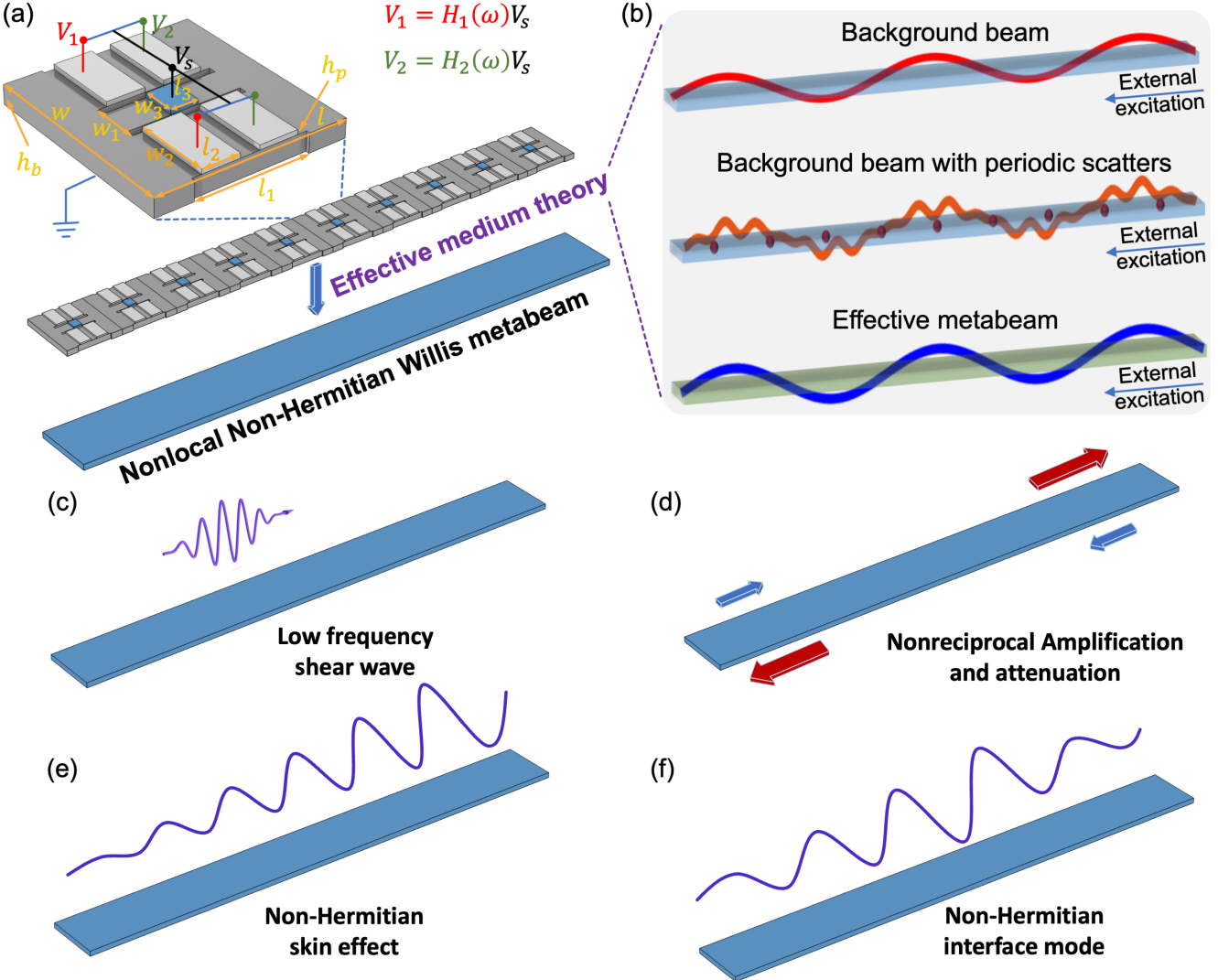


Figure 2: Schematic illustration of the EMT for a metabeam and its associated wave phenomena. (a) The unit cell of the metabeam, featuring a sensor (blue) and four actuators (light gray) in the top panel. The middle panel depicts a finite metabeam consisting of 10 unit cells, while the bottom panel presents its effective medium representation as a nonlocal Non-Hermitian Willis metabeam. (b) A schematic diagram illustrating the wave responses in different configurations: the top panel shows the response of the background beam, the middle panel includes periodic scatterers embedded in the background beam, and the bottom panel represents the response of the homogenized effective beam, all under external excitation (blue arrow). (c–f) Demonstrations of various phenomena of the nonlocal Non-Hermitian Willis metabeam: (c) low-frequency shear wave propagation, (d) nonreciprocal wave amplification and attenuation, (e) the non-Hermitian skin effect, and (f) the non-Hermitian interface mode.

transverse displacement  $w$  satisfy the following geometric relations (Yao et al., 2009; Chen et al., 2020)

$$\begin{aligned}\kappa &= \partial_x\psi + p \\ \gamma &= \partial_xw - \psi + s,\end{aligned}\tag{2}$$

106 where  $p$  and  $s$  represent the external curvature load and shear load, respectively. The general constitutive relation  
107 of the Timoshenko beam is given by (Yao et al., 2009; Chen et al., 2020)

$$\begin{bmatrix} \kappa \\ \gamma \\ \mu \\ J \end{bmatrix} = \begin{bmatrix} 1/D_0 & 0 & 0 & 0 \\ 0 & 1/G_0 & 0 & 0 \\ 0 & 0 & \rho_0 & 0 \\ 0 & 0 & 0 & I_0 \end{bmatrix} \begin{bmatrix} M \\ F \\ \partial_t w \\ \partial_t \psi \end{bmatrix}, \quad (3)$$

108 where  $D_0$  is the bending stiffness,  $G_0$  is the shear stiffness,  $I_0$  is the moment of inertia, and  $\rho_0$  is the line mass density.

109 These parameters are defined as  $D_0 = EI$ ,  $G_0 = k_s AG$ ,  $I_0 = \rho I$ , and  $\rho_0 = \rho A$ , where  $A$  is the cross-sectional area,

110  $k_s$  is the Timoshenko shear coefficient (taken as 5/6),  $I$  is the second moment of area, and  $\rho$  is the material density.

111 Using Eqs. (1), (2), and (3), the governing equations can be written in matrix form for the state vector

$$\zeta_1 \mathbf{u} = \mathbf{Q}, \quad (4)$$

112 where

$$\zeta_1 = \begin{bmatrix} 1/D_0 & 0 & 0 & -\partial_x \\ 0 & 1/G_0 & -\partial_x & 1 \\ 0 & \partial_x & -\rho_0 \partial_t^2 & 0 \\ \partial_x & 1 & 0 & -I_0 \partial_t^2 \end{bmatrix}, \quad \mathbf{u} = \begin{bmatrix} M \\ F \\ w \\ \psi \end{bmatrix}, \quad \mathbf{Q} = \begin{bmatrix} p \\ s \\ f \\ q \end{bmatrix}. \quad (5)$$

113 Meanwhile, Eq. (4) in the frequency domain  $e^{-i\omega t}$  is

$$\zeta_2 \mathbf{u} = \mathbf{Q}, \quad (6)$$

114 and in frequency-wavenumber domain  $e^{i(kx-\omega t)}$  is

$$\zeta \mathbf{u} = \mathbf{Q}, \quad (7)$$

115 where

$$\zeta_2 = \begin{bmatrix} 1/D_0 & 0 & 0 & -\partial_x \\ 0 & 1/G_0 & -\partial_x & 1 \\ 0 & \partial_x & \omega^2 \rho_0 & 0 \\ \partial_x & 1 & 0 & \omega^2 I_0 \end{bmatrix}, \quad \zeta = \begin{bmatrix} 1/D_0 & 0 & 0 & -ik \\ 0 & 1/G_0 & -ik & 1 \\ 0 & ik & \omega^2 \rho_0 & 0 \\ ik & 1 & 0 & \omega^2 I_0 \end{bmatrix} \quad (8)$$

## 116 2.2. Response of the background beam under external sources

117 Under the external excitation  $e^{i(kx-\omega t)}$  shown in the top panel of Fig. 2(b), the governing equations for the state

118 vector of a homogeneous background beam with external sources in the frequency-wavenumber domain are given by

119 (Chen et al., 2020)

$$\zeta \mathbf{u}_{\text{ext}} = \mathbf{Q}_{\text{ext}}, \quad (9)$$

120 where the subscript ext denotes the fields in Eq. (7) under external excitation.

121 2.3. Response of the effective metabeam under external sources

122 For the background beam with periodic scatterers under external excitation, as shown in the middle panel of Fig.  
 123 2(b), the response consists of the intrinsic behavior of the background beam and multiple scattering effects induced  
 124 by the periodic scatterers. In this setup, actuators generate a source vector, making the scatterers function similarly  
 125 to external sources.

126 In the homogenization process, the source vector applied by the actuators is represented as an effective source  
 127 vector  $\mathbf{Q}_{\text{eff}}$ . The governing equations for the state vector of the effective metabeam are then given by (Chen et al.,  
 128 2020)

$$\zeta \mathbf{u}_{\text{eff}} + \mathbf{Q}_{\text{eff}} = \mathbf{Q}_{\text{ext}}. \quad (10)$$

129 Here,  $\mathbf{Q}_{\text{eff}}$  is an unknown vector dependent on the local response at the microscopic scale and the multiple scattering  
 130 effects at the mesoscale, both of which are discussed in the following sections.

131 2.4. Local response at microscopic scale

132 The sensor-actuator elements detect the local state vector  $\mathbf{u}_{\text{loc}}$  and apply the source vector  $\mathbf{Q}_0$  to the beam. The  
 133 geometry and material parameters are presented in Appendix A. In our design (Fig. 2(a)), the sensor detects only  
 134 the bending curvature, while four actuators apply the bending moment and shear strain. However, this framework  
 135 can be extended to systems capable of detecting the complete local state vector and applying the full source vector.  
 136 In the frequency domain, the local source vector is related to the local state vector through the polarizability tensor,  
 137 modulated by the transfer functions  $H_1(\omega)$  and  $H_2(\omega)$ , as shown in Fig. 2(a) (Chen et al., 2020),

$$\mathbf{Q}_0 = \boldsymbol{\beta}(\omega) \mathbf{u}_{\text{loc}}. \quad (11)$$

138 The tensor  $\boldsymbol{\beta}(\omega)$  is a frequency-dependent local polarizability tensor, with only  $\beta_{11}$  and  $\beta_{21}$  being nonzero in our  
 139 design, as shown in Fig. 2(a). It is directly linked to the transfer functions implemented via analog or digital circuits  
 140 but cannot be determined analytically. Instead, we obtain it using the retrieval method described in the Appendix  
 141 E.

142 As shown in Fig. 2(a), the transfer function defines the relationship between the sensed voltage  $V_s$  from the  
 143 sensing piezoelectric patch and the actuator voltages  $V_1$  and  $V_2$ , given by

$$\begin{aligned} V_1 &= H_1(\omega) V_s, \\ V_2 &= H_2(\omega) V_s. \end{aligned} \quad (12)$$

144 Here,  $V_s = \int_A D_z dA / C_0$ , where  $A$  is the top surface area of the sensing piezoelectric patch,  $D_z$  is the  $z$ -component  
 145 of the electric displacement vector, and  $C_0$  is the capacitance, provided in Appendix A. An example of transfer  
 146 function implementation is detailed in Chen et al. (2021).

147 In general, a transfer function is expressed as the ratio of two complex polynomials. For instance, the transfer  
 148 functions  $H_1(\omega)$  and  $H_2(\omega)$  in this study can be written as

$$H_i(\omega) = \frac{\sum_{m=0}^M a_{m,i} \omega^m}{\sum_{n=0}^N b_{n,i} \omega^n}, \quad i = 1, 2, \quad (13)$$

where  $M$  and  $N$  are the highest-order indices, and  $a_{m,i}$  and  $b_{n,i}$  are the complex coefficients of the  $m$ th and  $n$ th order terms in the numerator and denominator polynomials of  $H_i(\omega)$ , respectively. The local polarizability tensor is not directly proportional to the transfer functions; however, its elements remain rational functions, as indicated by our observations and supported by the strong agreement between EMT predictions and COMSOL simulations. Consequently, the element in the  $i$ th row and  $j$ th column can be expressed as

$$\beta_{ij}(\omega) = \frac{\sum_{m=0}^M \tilde{a}_{m,ij}\omega^m}{\sum_{n=0}^N \tilde{b}_{n,ij}\omega^n}, \quad i, j = 1, 2, 3, 4, \quad (14)$$

where  $M$  and  $N$  denote the highest-order indices, and  $\tilde{a}_{m,ij}$  and  $\tilde{b}_{n,ij}$  are the complex coefficients of the  $m$ th and  $n$ th order terms in the numerator and denominator polynomials of  $\beta_{ij}(\omega)$ , respectively. By leveraging circuit-based control, each element can be modulated independently, allowing for the realization of an arbitrary local constitutive matrix that encompasses frequency-dependent responses, positive and negative values, real and imaginary components, and non-Hermitian configurations.

### 2.5. Multiple scattering at mesoscopic scale

Next, we analyze the multiple scattering effect in the middle panel of Fig. 2(b). Using Eq. (B.18), the state vector response at position  $x$  due to a point source  $\mathbf{Q}(x') = \delta(x' - nL)\mathbf{Q}_n$  located at  $x' = nL$  is given by

$$\mathbf{u}(x) = \mathbf{G}(\omega, x - nL)\mathbf{Q}_n. \quad (15)$$

where the Green's function in the frequency domain is defined in Eq. (B.16).

The system in this study is periodic, allowing Bloch's theorem to be applied to all fields, including the source vector  $\mathbf{Q}_n$  (Sieck et al., 2017). Therefore, the source vector  $\mathbf{Q}_n$  satisfies

$$\mathbf{Q}_n = e^{iknL}\mathbf{Q}_0. \quad (16)$$

Therefore, the total local field  $\mathbf{u}_{\text{loc}}$  at  $x = 0$ , excited by all sources, is the superposition of the local fields generated by each individual internal source and the external field  $\mathbf{u}_{\text{ext}}$

$$\mathbf{u}_{\text{loc}} = \mathbf{u}_{\text{ext}} + \sum_{n \in \mathbb{Z}} \mathbf{G}(\omega, 0 - nL)\mathbf{Q}_n = \mathbf{u}_{\text{ext}} + \mathbf{S}(\omega, k)\mathbf{Q}_0, \quad (17)$$

where the scattering matrix is defined as

$$\mathbf{S}(\omega, k) = \sum_{n \in \mathbb{Z}} \mathbf{G}(\omega, 0 - nL)e^{iknL}. \quad (18)$$

Here, the summation includes the current scatter at  $n = 0$ , unlike previous studies that exclude it to prevent divergence (Li et al., 2024). In our case, the Green's function remains finite at  $n = 0$ . Moreover, removing the effect of the current scatter violates the symmetry constraints in Eqs. (33–37) derived from macroscopic theory. By applying the symmetry condition of the Green's function in Eq. (C.6), we find that the scattering matrix  $\mathbf{S}$  satisfies

<sup>172</sup> the following symmetry properties:

$$\begin{aligned}\mathbf{S}(\omega, k) &= \mathbf{S}^\dagger(\omega, k), \\ \mathbf{S}(\omega, k) &= \mathbf{S}^T(\omega, -k), \\ \mathbf{S}(\omega, k) &= \mathbf{S}^*(-\omega, -k).\end{aligned}\tag{19}$$

<sup>173</sup> Applying Bloch's theorem to the source vector  $\mathbf{Q}_n$  in Eq. (16), the scattering matrix becomes

$$\begin{aligned}\mathbf{S}(\omega, k) &= \sum_{n \in \mathbb{Z}} \left[ \mathbf{R}_1(-nL) \mathbf{B}_1(-nL)^T e^{-i|nL|k_1} e^{iknL} + \mathbf{R}_2(-nL) \mathbf{B}_2(-nL)^T e^{-|nL|k_2} e^{iknL} \right] \\ &= \mathbf{R}_1(1) \mathbf{B}_1(1)^T \left( \sum_{n=-\infty}^{-1} e^{i(k_1+k)nL} + \frac{1}{2} \right) + \mathbf{R}_1(-1) \mathbf{B}_1(-1)^T \left( \sum_{n=1}^{\infty} e^{i(k-k_1)nL} + \frac{1}{2} \right) \\ &\quad + \mathbf{R}_2(1) \mathbf{B}_2(1)^T \left( \sum_{n=-\infty}^{-1} e^{(k_2+ik)nL} + \frac{1}{2} \right) + \mathbf{R}_2(-1) \mathbf{B}_2(-1)^T \left( \sum_{n=1}^{\infty} e^{(ik-k_2)nL} + \frac{1}{2} \right) \\ &= \mathbf{R}_1(1) \mathbf{B}_1(1)^T \left( \frac{e^{-iL(k_1+k)}}{1 - e^{-iL(k_1+k)}} + \frac{1}{2} \right) + \mathbf{R}_1(-1) \mathbf{B}_1(-1)^T \left( \frac{e^{iL(k-k_1)}}{1 - e^{iL(k-k_1)}} + \frac{1}{2} \right) \\ &\quad + \mathbf{R}_2(1) \mathbf{B}_2(1)^T \left( \frac{e^{-L(k_2+ik)}}{1 - e^{-L(k_2+ik)}} + \frac{1}{2} \right) + \mathbf{R}_2(-1) \mathbf{B}_2(-1)^T \left( \frac{e^{L(ik-k_2)}}{1 - e^{L(ik-k_2)}} + \frac{1}{2} \right).\end{aligned}\tag{20}$$

<sup>174</sup> Here,  $\mathbf{R}_1(x)$ ,  $\mathbf{R}_2(x)$ ,  $\mathbf{B}_1(x)$ , and  $\mathbf{B}_2(x)$  only depend on the sign of the spatial coordinate  $x$ . Therefore, their values at <sup>175</sup>  $x = 1$  are used to represent them for positive  $x$ , while their values at  $x = -1$  are used to represent them for negative <sup>176</sup>  $x$ . In the final step, the geometric series is used

$$\sum_{n=1}^{\infty} y^n = \lim_{N \rightarrow \infty} \sum_{n=1}^N y^n = \lim_{N \rightarrow \infty} \frac{y - y^{N+1}}{1 - y}.\tag{21}$$

<sup>177</sup> The series converges only if the common ratio satisfies  $|y| < 1$ . Strictly speaking, the magnitude of the common <sup>178</sup> ratio is equal to 1, causing the series to diverge. In this study, we directly neglect the divergent term  $y^{N+1}$ . This <sup>179</sup> approach can be justified by introducing small damping, allowing the wavenumber to have a small imaginary part <sup>180</sup> such that the common ratio satisfies  $|y| < 1$  (Sieck et al., 2017; Shore and Yaghjian, 2007). Subsequently, the limit <sup>181</sup> is taken as the damping approaches zero. This procedure is also validated a posteriori, as the dispersion relations <sup>182</sup> obtained from the effective media closely match those from COMSOL simulation.

## <sup>183</sup> 2.6. Effective constitutive relations

<sup>184</sup> Next, we derive the effective constitutive relations. Eliminating the external excitation from Eqs. (9) and (10) <sup>185</sup> gives

$$\zeta (\mathbf{u}_{\text{eff}} - \mathbf{u}_{\text{ext}}) = -\mathbf{Q}_{\text{eff}}.\tag{22}$$

<sup>186</sup> Additionally, eliminating the local state vector  $\mathbf{u}_{\text{loc}}$  from Eq. (11) and (17) yields

$$(\mathbf{I} - \beta \mathbf{S}) \mathbf{Q}_0 = \beta \mathbf{u}_{\text{ext}},\tag{23}$$

<sup>187</sup> where  $\mathbf{I}$  is the  $4 \times 4$  identity matrix. Additionally, applying spatial averaging, the effective source vector  $\mathbf{Q}_{\text{eff}}$  relates  
<sup>188</sup> to the microscopic point source vector  $\mathbf{Q}_0$  at  $x = 0$  as (Sieck et al., 2017; Chen et al., 2020; Alù, 2011)

$$\mathbf{Q}_{\text{eff}} = \frac{1}{l} \int_{-l/2}^{l/2} \delta(x) \mathbf{Q}_0 dx = \frac{\mathbf{Q}_0}{l}, \quad (24)$$

<sup>189</sup> where  $l$  is the unit cell length. Using Eqs. (22)–(24), we derive the constitutive relation (detailed derivation in the  
<sup>190</sup> Appendix D)

$$\mathbf{Q}_{\text{eff}} = \mathbf{K} \mathbf{u}_{\text{eff}}, \quad (25)$$

<sup>191</sup> where

$$\mathbf{K} = [l\mathbf{I} - l\beta\mathbf{S} - \beta\zeta^{-1}]^{-1} \beta. \quad (26)$$

<sup>192</sup> If  $\beta$  is nonsingular, Eq. (26) simplifies to

$$\mathbf{K} = [l\beta^{-1} - L\mathbf{S} - \zeta^{-1}]^{-1}. \quad (27)$$

<sup>193</sup> when BD are nonzero In Section 2.4, we establish that the local polarizability matrix  $\beta$  can be an arbitrary frequency-  
<sup>194</sup> dependent but wavenumber-independent matrix. Here, we constrain it to be a real symmetric matrix and an even  
<sup>195</sup> function with respect to  $\omega$ . Given  $\zeta$  in Eq. (8),  $\mathbf{S}$  in Eq. (18), and  $\beta$  as a real even symmetric matrix, they satisfy  
<sup>196</sup> the following symmetry conditions

$$\begin{aligned} \zeta(\omega, k) &= \zeta^*(-\omega, -k), & \mathbf{S}(\omega, k) &= \mathbf{S}^*(-\omega, -k), & \beta(\omega, k) &= \beta^*(-\omega, -k), \\ \zeta(\omega, k) &= \zeta^\dagger(\omega, k), & \mathbf{S}(\omega, k) &= \mathbf{S}^\dagger(\omega, k), & \beta(\omega, k) &= \beta^\dagger(\omega, k), \\ \zeta(\omega, k) &= \zeta^T(\omega, -k), & \mathbf{S}(\omega, k) &= \mathbf{S}^T(\omega, -k), & \beta(\omega, k) &= \beta^T(\omega, -k). \end{aligned} \quad (28)$$

<sup>197</sup> Since matrix addition, subtraction, and inversion in Eq. (26) preserve these symmetries, the resulting matrix  $\mathbf{K}$  also  
<sup>198</sup> satisfies them.

<sup>199</sup> Substituting Eq. (25) into Eq. (10) in the absence of an external source and comparing it with Eq. (3), we  
<sup>200</sup> propose a general constitutive relation for Willis metabeams in matrix form

$$\begin{bmatrix} \kappa_{\text{eff}} \\ \gamma_{\text{eff}} \\ \mu_{\text{eff}} \\ J_{\text{eff}} \end{bmatrix} = \begin{bmatrix} 1/D_0 + K_{11} & K_{12} & K_{13}/(-i\omega) & K_{14}/(-i\omega) \\ K_{21} & 1/G_0 + K_{22} & K_{23}/(-i\omega) & K_{24}/(-i\omega) \\ K_{31}/(-i\omega) & K_{32}/(-i\omega) & \rho_0 + K_{33}/(-\omega^2) & K_{34}/(-\omega^2) \\ K_{41}/(-i\omega) & K_{42}/(-i\omega) & K_{43}/(-\omega^2) & I_0 + K_{44}/(-\omega^2) \end{bmatrix} \begin{bmatrix} M_{\text{eff}} \\ F_{\text{eff}} \\ v_{\text{eff}} \\ \varphi_{\text{eff}} \end{bmatrix}, \quad (29)$$

<sup>201</sup> Here,  $v_{\text{eff}}$  and  $\varphi_{\text{eff}}$  represent the velocity and angular velocity, respectively, satisfying  $v_{\text{eff}} = \dot{w}_{\text{eff}}$  and  $\varphi_{\text{eff}} = \dot{\psi}_{\text{eff}}$  in  
<sup>202</sup> the time domain, and  $v_{\text{eff}} = -i\omega w_{\text{eff}}$  and  $\varphi_{\text{eff}} = -i\omega \psi_{\text{eff}}$  in the frequency domain. Using these relations, we rewrite  
<sup>203</sup> Eq. (29) as

$$\begin{bmatrix} \boldsymbol{\varepsilon} \\ \mathbf{p} \end{bmatrix} = \begin{bmatrix} \mathbf{C} & \mathbf{B} \\ \mathbf{D} & \rho \end{bmatrix} \begin{bmatrix} \boldsymbol{\sigma} \\ \mathbf{v} \end{bmatrix} \quad (30)$$

204 where

$$\boldsymbol{\varepsilon} = \begin{bmatrix} \kappa_{\text{eff}} \\ \gamma_{\text{eff}} \end{bmatrix}, \mathbf{p} = \begin{bmatrix} \mu_{\text{eff}} \\ J_{\text{eff}} \end{bmatrix}, \boldsymbol{\sigma} = \begin{bmatrix} M_{\text{eff}} \\ F_{\text{eff}} \end{bmatrix}, \mathbf{v} = \begin{bmatrix} v_{\text{eff}} \\ \varphi_{\text{eff}} \end{bmatrix}, \quad (31)$$

205 and

$$\begin{aligned} \mathbf{C} &= \begin{bmatrix} -1/D_0 + K_{11} & K_{12} \\ K_{21} & 1/G_0 + K_{22} \end{bmatrix}, & \mathbf{B} &= \begin{bmatrix} K_{13}/(-i\omega) & K_{14}/(-i\omega) \\ K_{23}/(-i\omega) & K_{24}/(-i\omega) \end{bmatrix}, \\ \mathbf{D} &= \begin{bmatrix} K_{31}/(-i\omega) & K_{32}/(-i\omega) \\ K_{33}/(-i\omega) & K_{34}/(-i\omega) \end{bmatrix}, & \boldsymbol{\rho} &= \begin{bmatrix} \rho_0 + K_{33}/(-\omega^2) & K_{34}/(-\omega^2) \\ K_{43}/(-\omega^2) & I_0 + K_{44}/(-\omega^2) \end{bmatrix}. \end{aligned} \quad (32)$$

206 Equation (30) represents the effective constitutive relation in compliance form, where  $\mathbf{B}$  and  $\mathbf{D}$  are the Willis coupling  
207 matrices. The constitutive matrices satisfy the following conditions

$$\begin{aligned} \mathbf{C}(\omega, k) &= \mathbf{C}^*(-\omega, -k), & \mathbf{B}(\omega, k) &= \mathbf{B}^*(-\omega, -k), \\ \mathbf{D}(\omega, k) &= \mathbf{D}^*(-\omega, -k), & \boldsymbol{\rho}(\omega, k) &= \boldsymbol{\rho}^*(-\omega, -k), \end{aligned} \quad (33)$$

208

$$\mathbf{C}(\omega, k) = \mathbf{C}^\dagger(\omega, k), \quad \mathbf{B}(\omega, k) = -\mathbf{D}^\dagger(\omega, k), \quad \boldsymbol{\rho}(\omega, k) = \boldsymbol{\rho}^\dagger(\omega, k), \quad (34)$$

209

$$\mathbf{C}(\omega, k) = \mathbf{C}^T(\omega, -k), \quad \mathbf{B}(\omega, k) = \mathbf{D}^T(\omega, -k), \quad \boldsymbol{\rho}(\omega, k) = \boldsymbol{\rho}^T(\omega, -k), \quad (35)$$

210 Using Eq. (33) and Eq. (34), we obtain the following symmetry conditions

$$\mathbf{C}(\omega, k) = \mathbf{C}^T(-\omega, -k), \quad \mathbf{B}(\omega, k) = \mathbf{D}^T(-\omega, -k), \quad \boldsymbol{\rho}(\omega, k) = \boldsymbol{\rho}^T(-\omega, -k), \quad (36)$$

211 Furthermore, using Eq. (35) and Eq. (36), we obtain the following symmetry conditions

$$\mathbf{C}(\omega, k) = \mathbf{C}(-\omega, k), \quad \mathbf{B}(\omega, k) = \mathbf{B}(-\omega, k), \quad \mathbf{D}(\omega, k) = \mathbf{D}(-\omega, k), \quad \boldsymbol{\rho}(\omega, k) = \boldsymbol{\rho}(-\omega, k), \quad (37)$$

212 These five symmetry conditions are not independent; rather, Eq. (33), Eq. (36), and Eq. (37) serve as the  
213 fundamental ones in the macroscopic framework, while the remaining two follow from them. Eq. (33) arises from  
214 the requirement that all physical fields in classical physics be real-valued (Agranovich and Ginzburg, 2013; Shokri  
215 and Rukhadze, 2019). Eq. (36) represents the major symmetry of Willis materials, while Eq. (37) corresponds to  
216 time-reversal symmetry (Agranovich and Ginzburg, 2013; Shokri and Rukhadze, 2019; Altman and Suchy, 2011). Eq.  
217 (35) follows from the Maxwell-Betti reciprocity theorem, which itself derives from major symmetry and time-reversal  
218 symmetry (Agranovich and Ginzburg, 2013; Shokri and Rukhadze, 2019; Pernas-Salomón and Shmuel, 2020b).

219 Our sensor-actuator system can break these symmetry conditions, enabling the realization of unconventional  
220 symmetry-broken nonlocal Willis media. For instance, breaking time-reversal symmetry requires violating the cor-  
221 responding symmetry of the polarizability tensor, i.e.,  $\boldsymbol{\beta}(\omega) \neq \boldsymbol{\beta}(-\omega)$ , which can be achieved by implementing  
222 odd-frequency-dependent transfer functions. Breaking major symmetry or Maxwell-Betti reciprocity requires a non-  
223 Hermitian or asymmetric polarizability tensor. By tailoring the polarizability tensor at the microscopic level, EMT  
224 allows for the engineering of macroscopic media with arbitrary symmetry-breaking properties.

225 Here, material properties depend on both frequency and wavenumber, indicating that the Willis metabeam ex-

226 exhibits both frequency and spatial dispersion (Agranovich and Ginzburg, 2013). Frequency and wavenumber are  
 227 treated as independent variables, as discussed in Appendix F. In the spacetime domain, these dependencies trans-  
 228 late into nonlocal constitutive relations, which are expressed in convolution form (Agranovich and Ginzburg, 2013;  
 229 Jackson, 2012; Pernas-Salomón and Shmuel, 2020a).

$$\begin{bmatrix} \boldsymbol{\varepsilon}(t, x) \\ \mathbf{p}(t, x) \end{bmatrix} = \int_{-\infty}^t \int_{-\infty}^{\infty} \begin{bmatrix} \mathbf{C}(t, t'; x, x') & \mathbf{B}(t, t'; x, x') \\ \mathbf{D}(t, t'; x, x') & \boldsymbol{\rho}(t, t'; x, x') \end{bmatrix} \begin{bmatrix} \boldsymbol{\sigma}(t', x') \\ \mathbf{v}(t', x') \end{bmatrix} dt' dx' \quad (38)$$

230 If the medium's properties remain constant over time (time-independent), translational symmetry in the time domain  
 231 is preserved, making the constitutive matrix dependent only on the time difference  $t - t'$  (Agranovich and Ginzburg,  
 232 2013). Similarly, if the medium is spatially uniform, all points are equivalent, and the constitutive matrix depends  
 233 only on the spatial difference  $x - x'$  (Agranovich and Ginzburg, 2013). Under these conditions, we obtain

$$\begin{bmatrix} \boldsymbol{\varepsilon}(t, x) \\ \mathbf{p}(t, x) \end{bmatrix} = \int_{-\infty}^t \int_{-\infty}^{\infty} \begin{bmatrix} \mathbf{C}(t - t', x - x') & \mathbf{B}(t - t', x - x') \\ \mathbf{D}(t - t', x - x') & \boldsymbol{\rho}(t - t', x - x') \end{bmatrix} \begin{bmatrix} \boldsymbol{\sigma}(t', x') \\ \mathbf{v}(t', x') \end{bmatrix} dt' dx' \quad (39)$$

234 The quantity  $\Psi$ , representing  $\boldsymbol{\varepsilon}$ ,  $\mathbf{p}$ ,  $\mathbf{C}$ ,  $\mathbf{B}$ ,  $\mathbf{D}$ ,  $\boldsymbol{\rho}$ ,  $\boldsymbol{\sigma}$ , and  $\mathbf{v}$ , is related in real space and reciprocal space through the  
 235 Fourier transform

$$\Psi(t, x) = \frac{1}{2\pi} \int_{-\infty}^{\infty} \int_{-\infty}^{\infty} \Psi(\omega, k) e^{i(kx - \omega t)} dx dt \quad (40)$$

236 and its inverse transform,

$$\Psi(\omega, k) = \frac{1}{2\pi} \int_{-\infty}^{\infty} \int_{-\infty}^{\infty} \Psi(t, x) e^{-i(kx - \omega t)} dk dt \quad (41)$$

237 Since all wave fields in classical physics are real-valued in real space, the Fourier transform satisfies

$$\Psi(\omega, k) = \Psi^*(-\omega, -k). \quad (42)$$

238 This symmetry condition, imposed by physical constraints at the macroscopic scale, aligns with the microscopic  
 239 symmetries of the constitutive matrix in Eq. (33).

## 240 2.7. Governing equations and boundary value problem

241 In this section, we discuss the governing equations and the BVP. For the effective nonlocal non-Hermitian Willis  
 242 metabeam, the effective state vector remains governed by Eq. (1) and Eq. (2). Utilizing the constitutive relation in  
 243 Eq. (39), the governing equation for the state vector in the space-time domain is expressed as

$$\begin{bmatrix} 0 & -\partial_x \\ -\partial_x & 1 \end{bmatrix} \boldsymbol{\sigma}(t, x) + \int_{-\infty}^t \int_{-\infty}^{\infty} \mathbf{C}(t - t', x - x') \boldsymbol{\sigma}(t', x') + \mathbf{B}(t - t', x - x') \partial_t \mathbf{w}(t', x') dt' dx' = \mathbf{q}_1 \quad (43)$$

$$\begin{bmatrix} 0 & \partial_x \\ \partial_x & 1 \end{bmatrix} \mathbf{w}(t, x) + \partial_t \int_{-\infty}^t \int_{-\infty}^{\infty} \mathbf{D}(t - t', x - x') \boldsymbol{\sigma}(t', x') + \boldsymbol{\rho}(t - t', x - x') \partial_t \mathbf{w}(t', x') dt' dx' = \mathbf{q}_2 \quad (44)$$

245 where  $\mathbf{w} = [w, \psi]^T$ ,  $\mathbf{q}_1 = [p_{\text{ext}}, s_{\text{ext}}]^T$ , and  $\mathbf{q}_2 = [f_{\text{ext}}, q_{\text{ext}}]^T$ . In the frequency-wavenumber domain, the governing  
246 equations take the form

$$\mathbf{H}\mathbf{u}_{\text{eff}} = \mathbf{Q}_{\text{ext}}, \quad (45)$$

247 where

$$\mathbf{H} = \begin{bmatrix} 0 & 0 & 0 & -ik \\ 0 & 0 & -ik & 1 \\ 0 & ik & 0 & 0 \\ ik & 1 & 0 & 0 \end{bmatrix} + \begin{bmatrix} \mathbf{C} & -i\omega\mathbf{B} \\ -i\omega\mathbf{D} & -\omega^2\boldsymbol{\rho} \end{bmatrix}. \quad (46)$$

248 In the absence of an external source, the dispersion relations are obtained by setting the determinant of the coefficient  
249 matrix to zero

$$\det(\mathbf{H}) = 0. \quad (47)$$

250 For each  $\omega$  and  $k$  satisfying the dispersion relations, the corresponding solution  $\mathbf{u}_{\text{eff}}$  in Eq. (45) represents the  
251 eigenvector.

252 For the vibration problem, boundary conditions are required to determine the eigenfrequencies and eigenmodes of  
253 the metabeam. Based on the boundary conditions of the conventional Timoshenko beam, the most relevant boundary  
254 conditions for the nonlocal non-Hermitian Willis metabeam are listed below

$$\begin{aligned} \text{Fixed : } & \quad w_{\text{eff}} = 0, \quad \psi_{\text{eff}} = 0 \\ \text{Simply supported : } & \quad w_{\text{eff}} = 0, \quad M_{\text{eff}} = 0 \\ \text{Free : } & \quad M_{\text{eff}} = 0, \quad F_{\text{eff}} = 0 \end{aligned} \quad (48)$$

255 In our formalism of Willis media, the bending moment, shear force, displacement, and rotational angle are integrated  
256 into a state vector, allowing them to be directly prescribed as boundary conditions. This approach eliminates the  
257 challenges of the conventional Willis media framework, which involves second-order derivatives. In the traditional  
258 formulation, the nonlocal constitutive relations in Eq. (25) express the bending moment and shear force in terms  
259 of displacement and rotational angle, making their boundary conditions nonlocal. As a result, solving nonlocal  
260 boundary conditions analytically becomes intractable, requiring advanced numerical methods (Rabczuk et al., 2023).

### 261 3. Validation of the effective medium theory

262 In this section, we validate the EMT by comparing its predicted dispersion relations with those from unit cell  
263 analysis using COMSOL simulations across various transfer functions, including symmetric real, antisymmetric real,  
264 asymmetric real, frequency-dependent real, and antisymmetric imaginary cases. By accounting for spatial dispersion  
265 effects, the nonlocal EMT accurately captures wave behavior, including nonreciprocal propagation, attenuation, and  
266 amplification, even in high-frequency and short-wavelength regimes—where conventional homogenization theories  
267 often fail.

268 In our study, the sensing piezoelectric patch detects only the bending curvature, while the actuating piezoelectric  
269 patch applies only the bending moment and shear strain. Consequently, only  $\beta_{11}$  and  $\beta_{21}$  are nonzero in the local

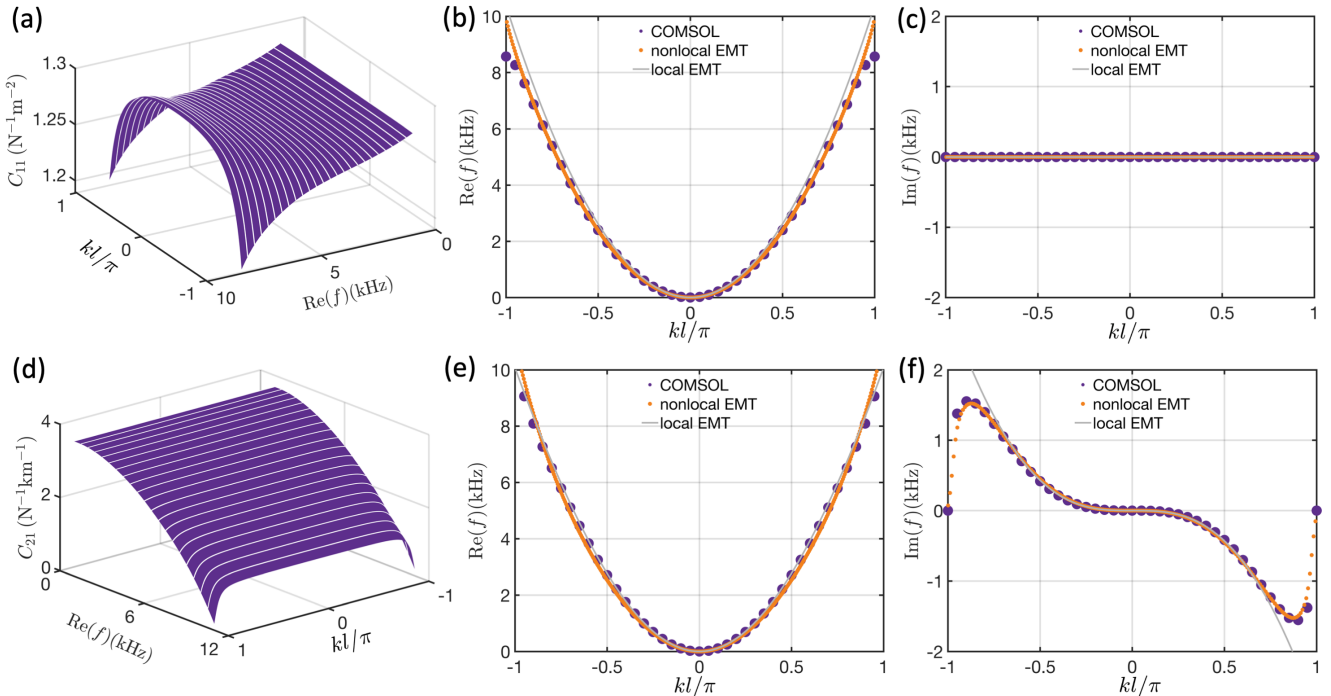


Figure 3: Effective material properties and dispersion relations for symmetric and antisymmetric real transfer functions. (a–c) Symmetric transfer functions: (a) Real part of  $C_{11}$  as a function of frequency and wavenumber. (b) Real part of the dispersion curves from unit cell analysis in COMSOL simulations (purple dots), nonlocal EMT (orange dots), and local EMT (gray solid line). (c) Imaginary part of the dispersion curves from COMSOL unit cell analysis (purple dots), nonlocal EMT (orange dots), and local EMT (gray solid line). (d–f) Antisymmetric transfer functions: (d) Real part of  $C_{21}$  as a function of frequency and wavenumber. (e) Real part of the dispersion curves from COMSOL unit cell analysis (purple dots), nonlocal EMT (orange dots), and local EMT (gray solid line). (f) Imaginary part of the dispersion curves from COMSOL unit cell analysis (purple dots), nonlocal EMT (orange dots), and local EMT (gray solid line).

<sup>270</sup> polarizability tensor. Under this condition, Eq. (26) simplifies to

$$C_{11} = \frac{1}{D_0} + K_{11} \quad (49)$$

$$C_{21} = K_{21},$$

<sup>271</sup> where

$$K_{11} = \frac{\beta_{11}(b_4k^4 + b_2k^2 + b_0)}{a_4k^4 + a_2k^2 + a_1k + a_0} \quad (50)$$

$$K_{21} = \frac{\beta_{21}(b_4k^4 + b_2k^2 + b_0)}{a_4k^4 + a_2k^2 + a_1k + a_0},$$

<sup>272</sup> and

$$b_4 = -D_0\beta_{11}g_0$$

$$b_2 = \omega^2(D_0\rho_0 + I_0g_0)$$

$$b_0 = \rho_0\omega^2(-I_0\omega^2 + g_0)$$

$$a_4 = D_0lg_0(-1 + S_{12}\beta_{21} + S_{11}\beta_{11}) \quad (51)$$

$$a_2 = -\omega^2(-D_0l\rho_0 - I_0lg_0 + D_0lS_{12}\beta_{21}\rho_0 + I_0lS_{12}\beta_{21}g_0 + D_0lS_{11}\beta_{11}\rho_0 + D_0I_0\beta_{11}g_0 + I_0lS_{11}\beta_{11}g_0)$$

$$a_1 = -D_0\beta_{21}g_0\omega^2\rho_0i$$

$$a_0 = -\omega^2\rho_0(-I_0\omega^2 + g_0)(-l + lS_{12}\beta_{21} + D_0\beta_{11} + lS_{11}\beta_{11}).$$

<sup>273</sup> As  $\omega \rightarrow 0$ , we also have  $k \rightarrow 0$ , reducing Eq. (50) to

$$C_{11} = \frac{1}{D_0} + \frac{\beta_{11}}{l - D_0\beta_{11}} \quad (52)$$

$$C_{21} = \frac{\beta_{21}}{l - D_0\beta_{11}},$$

<sup>274</sup> Here, the material properties become wavenumber-independent, reducing the medium to a local EMT, accurately  
<sup>275</sup> matching the dispersion relations in the low-frequency and long-wavelength regime. Additionally,  $\beta_{11}$  influences both  
<sup>276</sup>  $C_{11}$  and  $C_{21}$  simultaneously. For small  $\beta_{11}$ , the leading-order term is given by

$$C_{11} = \frac{1}{D_0} + \frac{\beta_{11}}{l} \quad (53)$$

$$C_{21} = \frac{\beta_{21}}{l}.$$

<sup>277</sup> In this case,  $\beta_{11}$  and  $\beta_{21}$  independently contribute to  $C_{11}$  and  $C_{21}$ , respectively.

<sup>278</sup> In Eq. (50),  $K_{11}$  and  $K_{21}$  are proportional to  $\beta_{11}$  and  $\beta_{21}$ , respectively, each scaled by a rational function. For a  
<sup>279</sup> symmetric transfer function where  $H_1(\omega) = H_2(\omega)$ , the actuators generate only bending moments, making  $\beta_{11}$  the  
<sup>280</sup> only nonzero component. Consequently,  $K_{11}$  is nonzero, modifying the effective bending stiffness in Eq. (30). For an  
<sup>281</sup> antisymmetric transfer function where  $H_1(\omega) = -H_2(\omega)$ , the actuators generate only shear strain, resulting in  $\beta_{21}$  as  
<sup>282</sup> the only nonzero component. In this case,  $K_{21}$  becomes nonzero, leading to the formation of effective shear stiffness  
<sup>283</sup> in Eq. (30). For an asymmetric transfer function, where  $H_1(\omega) \neq H_2(\omega)$  and  $H_1(\omega) \neq -H_2(\omega)$ , both  $K_{11}$  and  $K_{21}$   
<sup>284</sup> are generated simultaneously. Additionally, in our study, the imaginary part of the rational function is significantly  
<sup>285</sup> smaller than the real part. As a result, when the transfer functions  $H_1(\omega)$  and  $H_2(\omega)$  are purely real,  $K_{11}$  and  $K_{21}$

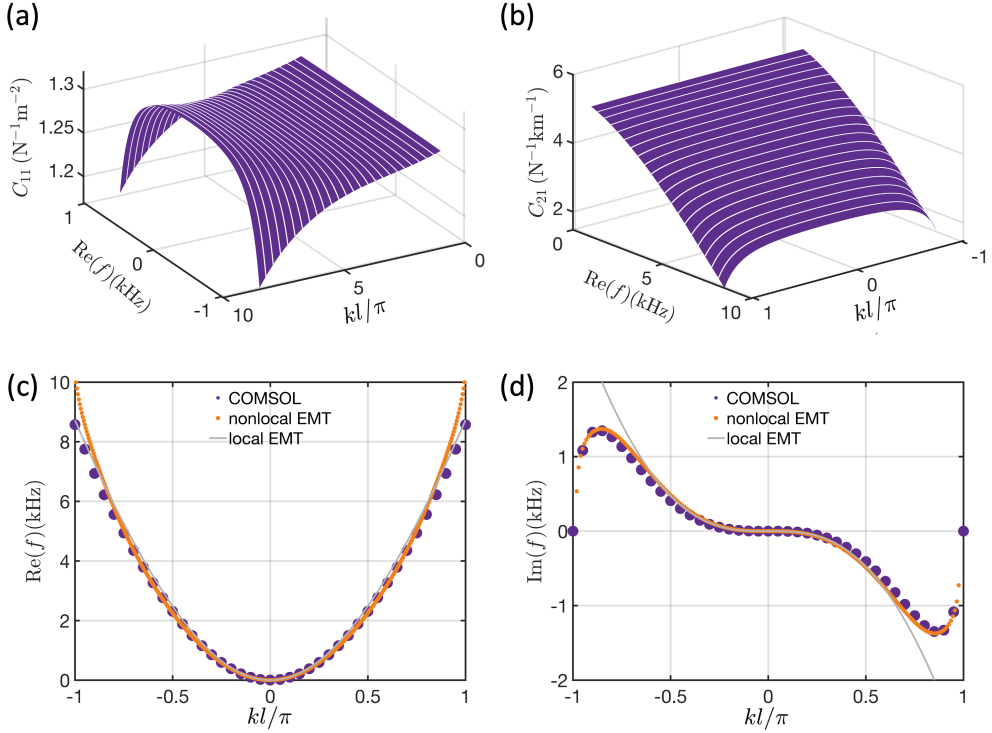


Figure 4: Effective material properties and dispersion relations for asymmetric real transfer functions. (a) Real part of  $C_{11}$  as a function of frequency and wavenumber. (b) Real part of  $C_{21}$  as a function of frequency and wavenumber. (c) Real part of the dispersion curves from unit cell analysis in COMSOL simulations (purple dots), nonlocal EMT (orange dots), and local EMT (gray solid line). (d) Imaginary part of the dispersion curves from COMSOL unit cell analysis (purple dots), nonlocal EMT (orange dots), and local EMT (gray solid line).

are nearly real. Similarly, when the transfer functions are purely imaginary,  $K_{11}$  and  $K_{21}$  are nearly imaginary. For complex transfer functions,  $K_{11}$  and  $K_{21}$  are generally complex-valued.

Next, we examine the effective properties and dispersion relations for different transfer functions. For symmetric transfer functions with  $H_1(\omega) = H_2(\omega) = 0.05$ , Fig. 3(a) presents the real part of  $C_{11}$ , while the imaginary part is omitted as it is negligibly small. The dispersion curves from COMSOL simulations, the nonlocal effective  $C_{11}$  from Eq. (49), and the local effective  $C_{11}$  from Eq. (52) are shown in Fig. 3(b,c). The dispersion curves from the local EMT align well with COMSOL simulations in the low-frequency and long-wavelength regimes but deviate at high frequencies and short wavelengths. In contrast, the nonlocal EMT provides a close match to the COMSOL results across both low- and high-frequency ranges, demonstrating its superior accuracy in capturing wave dynamics over a broader frequency and wavelength spectrum compared to the local EMT.

For antisymmetric transfer functions with  $H_1(\omega) = -H_2(\omega) = 0.3$ , the effective properties and dispersion curves are shown in Fig. 3(d-f). Only the real part of  $C_{21}$  is displayed, as the imaginary part remains small and is therefore omitted. The presence of a nonzero real  $C_{21}$  introduces an imaginary component in the dispersion curves. The local EMT accurately captures both the real and imaginary parts of the dispersion relations in the low-frequency and long-wavelength regimes, while the nonlocal EMT extends this accuracy to high frequencies and short wavelengths. The emergence of  $C_{21}$  breaks the major symmetry, rendering the medium non-Hermitian and introducing a nonzero imaginary component in the dispersion relation. Furthermore, the imaginary part of the dispersion relation is antisymmetric with respect to the wavenumber, leading to wave attenuation for left-propagating waves (neg-

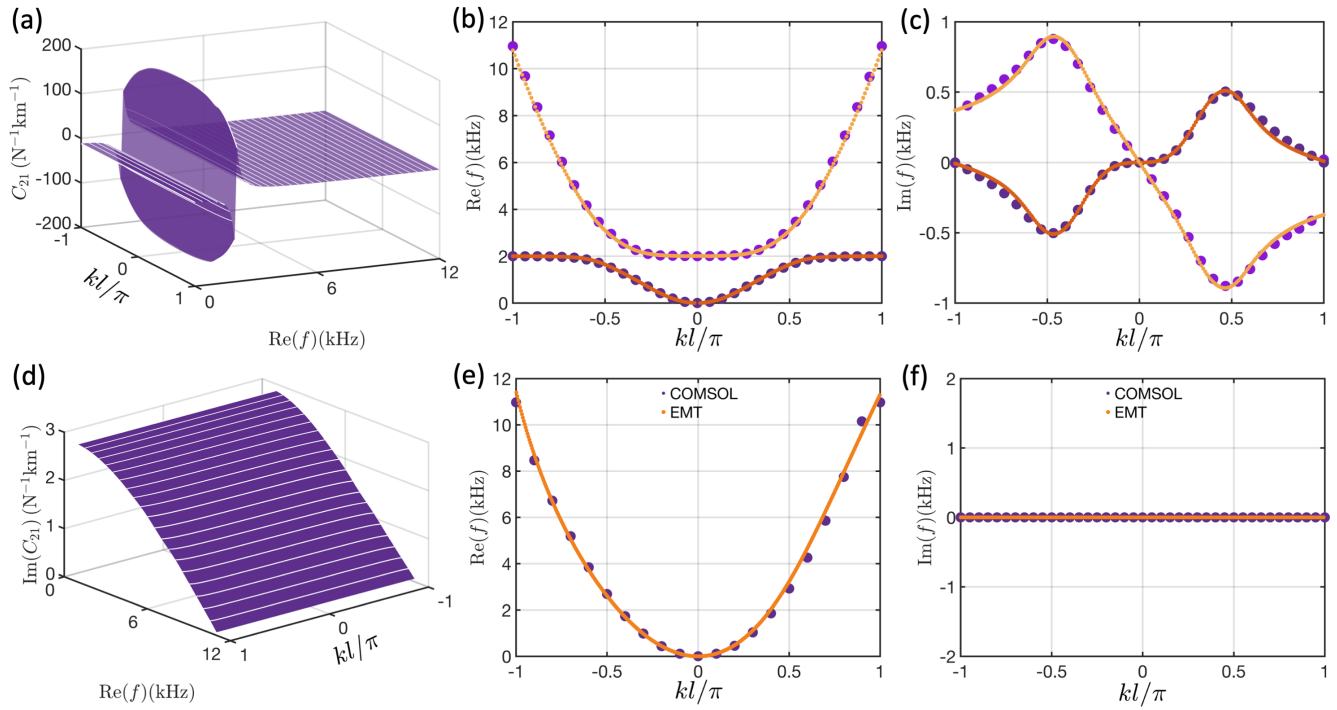


Figure 5: Effective material properties and dispersion relations for local resonant and antisymmetric imaginary transfer functions. (a–c) Local resonant transfer functions: (a) Real part of  $C_{11}$  as a function of frequency and wavenumber. (b) Real part of the dispersion curves from COMSOL unit cell analysis (dark purple dots for the lower band, light purple dots for the upper band) and from EMT (dark orange dots for the lower band, light orange dots for the upper band). (c) Imaginary part of the dispersion curves from COMSOL unit cell analysis (dark purple dots for the lower band, light purple dots for the upper band) and EMT (dark orange dots for the lower band, light orange dots for the upper band). (d–f) Antisymmetric imaginary transfer functions: (d) Real part of  $C_{21}$  as a function of frequency and wavenumber. (e) Real part of the dispersion curves from COMSOL unit cell analysis (purple dots) and EMT (orange dots). (f) Imaginary part of the dispersion curves from COMSOL unit cell analysis (purple dots) and EMT (orange dots).

304 tive wavenumber) and amplification for right-propagating waves (positive wavenumber). This asymmetry induces  
 305 nonreciprocal wave propagation due to non-Hermiticity.

306 For asymmetric transfer functions with  $H_1(\omega) = 0.35$  and  $H_2(\omega) = -0.25$ , which incorporate the effects of both  
 307 symmetric and antisymmetric transfer functions, the effective properties and dispersion curves are shown in Fig. 4.  
 308 In this case, both  $C_{11}$  and  $C_{21}$  are nonzero, resulting in a downward shift in the real part of the dispersion curve  
 309 and the appearance of an imaginary component in the dispersion relation. The local EMT accurately captures the  
 310 dispersion curves in the low-frequency and long-wavelength regimes but shows deviations at high frequencies and  
 311 short wavelengths. In contrast, the nonlocal EMT closely matches the COMSOL simulation results across both  
 312 regimes, demonstrating its effectiveness in capturing wave dynamics over a broader frequency and wavelength range.

313 Our EMT extends beyond constant transfer functions and applies to frequency-dependent transfer functions,  
 314 including the local resonant transfer function discussed here. We consider antisymmetric transfer functions given by

$$H_1(\omega) = -H_2(\omega) = \frac{0.3\omega_0^2}{\omega^2 - \omega_0^2} \quad (54)$$

315 where  $\omega_0 = 4000\pi$  Hz. In this case,  $H_1(\omega)$  is negative for  $\omega < \omega_0$ , positive for  $\omega > \omega_0$ , and singular at  $\omega = \omega_0$ .  
 316 The antisymmetric transfer function induces a nonzero  $C_{21}$ , breaking Hermiticity and resulting in nonzero imaginary  
 317 dispersion curves. The presence of local resonance splits the dispersion curve into two branches, with the imaginary  
 318 dispersion curves exhibiting frequency sign reversal due to the sign change of  $C_{21}$  at  $\omega_0$ . The nonlocal EMT closely

<sup>319</sup> matches the COMSOL simulation results for both real and imaginary dispersion curves across high-frequency and  
<sup>320</sup> short-wavelength regimes, as shown in Fig. 5(a-c), demonstrating its effectiveness in capturing wave dynamics for  
<sup>321</sup> frequency-dependent transfer functions over a broad frequency and wavelength range.

<sup>322</sup> Non-Hermiticity alone does not necessarily lead to a complex spectrum. For instance, eigenvalues remain real in  
<sup>323</sup> the PT-unbroken phase and can also be real in a more general pseudo-Hermitian system (Ashida et al., 2020). In our  
<sup>324</sup> system, verifying the pseudo-Hermitian condition is challenging, yet we observe a real spectrum for antisymmetric  
<sup>325</sup> imaginary transfer functions. For transfer functions  $H_1(\omega) = -H_2(\omega) = 0.3i$ , Fig. 5(d) presents the imaginary part  
<sup>326</sup> of  $C_{21}$ , while the real part is omitted as it is negligibly small. The nonzero  $C_{21}$  breaks the Hermitian condition,  
<sup>327</sup> yet the spectra in Fig. 5(e,f) remain purely real. However, the real part of the dispersion curve is asymmetric with  
<sup>328</sup> respect to the vertical axis, as the nonzero  $C_{21}$  breaks parity symmetry. The agreement between the dispersion  
<sup>329</sup> curves from COMSOL simulations and EMT in Fig. 5(e) confirms this asymmetry, demonstrating the validity of  
<sup>330</sup> EMT for purely imaginary transfer functions.

#### <sup>331</sup> 4. Wave phenomena in non-Hermitian Willis beam

##### <sup>332</sup> 4.1. Dispersion curves and mode characterization of flexural waves

<sup>333</sup> **Flexural wave characterization+Physical mechanism** In our study, only  $K_{21}$  and  $K_{11}$  are nonzero. Thus, the  
<sup>334</sup> dispersion equations in Eq. (45) simplify to

$$\begin{pmatrix} C_{11} & 0 & 0 & -k i \\ C_{21} & 1/G_0 & -k i & 1 \\ 0 & k i & \omega^2 \rho_0 & 0 \\ k i & 0 & 0 & J_0 \omega^2 \end{pmatrix} \begin{pmatrix} M_{\text{eff}} \\ F_{\text{eff}} \\ w_{\text{eff}} \\ \psi_{\text{eff}} \end{pmatrix} = \begin{pmatrix} 0 \\ 0 \\ 0 \\ 0 \end{pmatrix} \quad (55)$$

<sup>335</sup> where  $C_{11}$  and  $C_{21}$  are defined in Eq. (49). Eliminate  $M_{\text{eff}}$  and  $F_{\text{eff}}$  gives

$$\begin{bmatrix} -C_{11}(-\omega^2 \rho_0 + G_0 k^2) & -G_0 k(C_{11}i - C_{21}k) \\ C_{11}G_0 k i & -C_{11}G_0 + C_{11}J_0 \omega^2 - C_{21}G_0 k i - k^2 \end{bmatrix} \begin{bmatrix} w_{\text{eff}} \\ \psi_{\text{eff}} \end{bmatrix} = \begin{bmatrix} 0 \\ 0 \end{bmatrix} \quad (56)$$

<sup>336</sup> Assuming  $w_{\text{eff}}$  as 1, we have

$$\psi_{\text{eff}} = -\frac{C_{11}G_0 k i}{C_{11}G_0 - C_{11}J_0 \omega^2 + C_{21}G_0 k i + k^2} \quad (57)$$

<sup>337</sup> The ratio of shear strain and rotation angle is defined as

$$\frac{\gamma_{\text{eff}}}{\psi_{\text{eff}}} = \frac{i k w_{\text{eff}} - \psi_{\text{eff}}}{\psi_{\text{eff}}} = -\frac{(C_{11}i - C_{21}k)(-C_{11}\omega^2 \rho_0 + 2C_{11}G_0 k^2 + C_{21}G_0 k^3 i)}{C_{11}(-\omega^2 \rho_0 + G_0 k^2)(C_{11} + C_{21}k i)i} \quad (58)$$

<sup>338</sup> As shown in Fig. 6, the magnitude of the ratio of shear strain to rotation angle increases significantly compared to the  
<sup>339</sup> traditional Timoshenko beam model, making the shear effect observable when  $C_{21}$  is nonzero for the antisymmetric  
<sup>340</sup> transfer functions  $H_1 = -H_2 = -1$ . This indicates that the Willis metabeam in our study can support shear waves  
<sup>341</sup> at low frequencies, a feature absent in classical beam models.

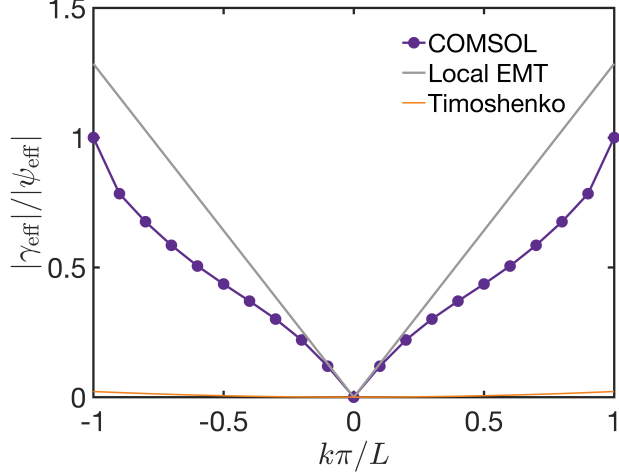


Figure 6: The magnitude of the ratio of shear strain to rotation angle from COMSOL simulations (purple solid line with circles), local EMT (gray solid line), and the traditional Timoshenko beam model (orange solid line). Here, antisymmetric transfer functions  $H_1 = -H_2 = 1$  are used.

#### 342 4.2. The broken reciprocity theorem

343 In local media, the reciprocity theorem is equivalent to major symmetry (Nassar et al., 2020). However, in  
 344 nonlocal media, major symmetry alone does not ensure reciprocity. Instead, reciprocity arises from the combined  
 345 presence of major symmetry and time-reversal symmetry (Shokri and Rukhadze, 2019). In our system, the presence  
 346 of  $C_{21}$  breaks major symmetry, leading to reciprocity violation. Next, we examine reciprocity and its breaking,  
 347 starting with the Green's function. The Green's function of Willis metabeam in the frequency-wavenumber domain  
 348 satisfies

$$\mathbf{HG}_{\text{eff}}(\omega, k) = \mathbf{I}. \quad (59)$$

349 The presence of  $C_{21}$  breaks the symmetry condition of  $\mathbf{H}$ .

$$\mathbf{H}(\omega, k) \neq \mathbf{H}^T(\omega, -k), \quad (60)$$

350 Therefore, the Green's function  $\mathbf{G}_{\text{eff}} = \mathbf{H}^{-1}$  no longer satisfies the symmetry condition

$$\mathbf{G}_{\text{eff}}(\omega, k) \neq \mathbf{G}_{\text{eff}}^T(\omega, -k), \quad (61)$$

351 which translates to

$$\mathbf{G}_{\text{eff}}(\omega, x - x') \neq \mathbf{G}_{\text{eff}}^T(\omega, x' - x) \quad (62)$$

352 in the spatial domain. For an external load  $\mathbf{Q}_{\text{ext}}$ , the corresponding response is given by

$$\mathbf{u}_{\text{eff}}(\omega, x) = \int_L \mathbf{G}_{\text{eff}}(\omega, x - x') \mathbf{Q}_{\text{ext}}(x') dx' \quad (63)$$

353 in the spatial domain. To evaluate the reciprocity condition, we conduct two load-response tests. In the first case, the  
 354 applied load is  $\mathbf{Q}_{\text{ext}}^1(\omega, x)$  with the corresponding response  $\mathbf{u}_{\text{eff}}^1(\omega, x)$ , while in the second case, the load is  $\mathbf{Q}_{\text{ext}}^2(\omega, x)$

355 with the response  $\mathbf{u}_{\text{eff}}^2(\omega, x)$ . The reciprocity condition is given by (Nassar et al., 2020)

$$\int_L (\mathbf{u}_{\text{eff}}^2)^T(\omega, x) \mathbf{Q}_{\text{ext}}^1(\omega, x) dx = \int_L (\mathbf{u}_{\text{eff}}^1)^T(\omega, x) \mathbf{Q}_{\text{ext}}^2(\omega, x) dx. \quad (64)$$

356 Using Eq. (62), the reciprocity condition can be rewritten as

$$\int_L \int_L (\mathbf{Q}_{\text{ext}}^2)^T(\omega, x') \mathbf{G}_{\text{eff}}^T(\omega, x - x') \mathbf{Q}_{\text{ext}}^1(\omega, x) dx dx' = \int_L \int_L (\mathbf{Q}_{\text{ext}}^1)^T(\omega, x') \mathbf{G}_{\text{eff}}^T(\omega, x - x') \mathbf{Q}_{\text{ext}}^2(\omega, x) dx dx'. \quad (65)$$

357 Taking the transpose and interchanging  $x$  and  $x'$  on the right-hand side, we obtain

$$\int_L \int_L (\mathbf{Q}_{\text{ext}}^2)^T(\omega, x') \mathbf{G}_{\text{eff}}^T(\omega, x - x') \mathbf{Q}_{\text{ext}}^1(\omega, x) dx dx' = \int_L \int_L (\mathbf{Q}_{\text{ext}}^2)^T(\omega, x') \mathbf{G}_{\text{eff}}(\omega, x' - x) \mathbf{Q}_{\text{ext}}^1(\omega, x) dx dx'. \quad (66)$$

358 Therefore, Eq. (66) shows that the reciprocity condition in Eq. (64) is equivalent to the symmetry condition of the  
359 Green's function,

$$\mathbf{G}_{\text{eff}}(\omega, x - x') = \mathbf{G}_{\text{eff}}^T(\omega, x' - x). \quad (67)$$

360 In our study, the presence of  $C_{21}$  breaks this symmetry condition, leading to the inequality in Eq. (62). As a result,  
361 the equality in Eq. (66) is violated, thereby breaking the reciprocity theorem in Eq. (64).

362 We now numerically verify the breaking of the reciprocity theorem using COMSOL simulations with constant  
363 antisymmetric transfer functions  $H_1(\omega) = -H_2(\omega) = 0.3$ . Two numerical tests are performed: in the first case, a  
364 unit shear force  $\mathbf{Q}_{\text{ext}}^1(x) = [0, 0, 0, 1]^T \delta(x + 6l)$  is applied at  $x = -6l$ , and the resulting displacement  $w_1$  is measured  
365 at  $x = 6l$ , as shown in Fig. 7(a). In the second case, a unit shear force  $\mathbf{Q}_{\text{ext}}^2(x) = [0, 0, 0, 1]^T \delta(x - 6l)$  is applied at  
366  $x = 6l$ , and the displacement  $w_2$  is measured at  $x = -6l$ , as illustrated in Fig. 7(a). The difference between the  
367 left-hand side and right-hand side of Eq. (64) is given by

$$\Delta = (\mathbf{u}_{\text{eff}}^2)^T \mathbf{Q}_{\text{ext}}^1 - (\mathbf{u}_{\text{eff}}^1)^T \mathbf{Q}_{\text{ext}}^2 = w_2 - w_1. \quad (68)$$

368 The measured magnitude of  $\Delta$ , normalized by  $|w_2|$ , as a function of frequency is shown in Fig. 7(b). Since  $|\Delta|/|w_1|$   
369 is nonzero,  $\Delta$  does not vanish, confirming the violation of the reciprocity theorem.

370 For a shear load applied on the left, the wave in the metabeam undergoes attenuation. This attenuation can be  
371 characterized using the  $k$ - $\omega$  dispersion relations. By sweeping  $\omega$  from 1 kHz to 10 kHz, the corresponding  $k$  values  
372 are obtained by solving Eq. (47). The resulting dispersion curves are shown in Fig. 7(c) (3D view), Fig. 7(d) (front  
373 view), and Fig. 7(e) (top view). As an example, at an excitation frequency of 4 kHz, the imaginary parts of both  
374 wavenumbers are positive, indicating wave attenuation in the metabeam, as shown in the top panel of Fig. 7(a).  
375 Furthermore, in Fig. 7(f), the imaginary wavenumber matches the decay factor observed in the logarithmic plot of  
376 the transverse displacement magnitude, confirming the attenuation behavior.

#### 377 4.3. Bulk-boundary correspondence

378 In Hermitian systems, the governing operator is Hermitian, ensuring real eigenvalues. In classical elasticity, for  
379 example, the governing equation can be expressed as an eigenvalue problem in Hilbert space, where the Hermitian

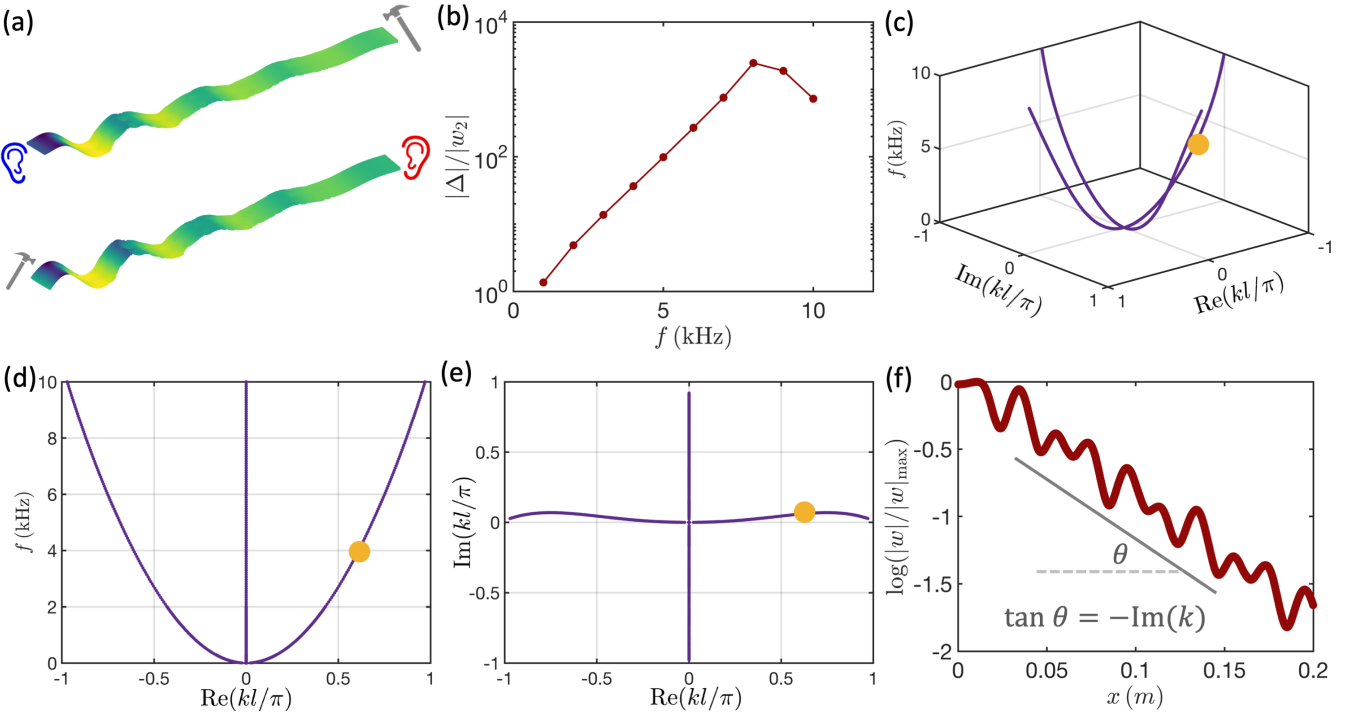


Figure 7: Nonreciprocal wave propagation in Willis media. (a) Displacement response under two shear force loads applied at the right (top panel) and left (bottom panel) with an excitation frequency of 4 kHz. The corresponding displacements are measured at the opposite ends. (b) Normalized displacement difference as a function of excitation frequency. (c) 3D view of the  $k$ - $\omega$  dispersion curves, where the orange point corresponds to the excitation frequency of 4 kHz in the bottom panel of (a). (d) Front view of the  $k$ - $\omega$  dispersion curves. (e) Top view of the  $k$ - $\omega$  dispersion curves. (f) Displacement field extracted along the middle line of the bottom panel in (a), with the slope of the gray solid line corresponding to the imaginary part of the orange point in (e).

380 nature of the operator guarantees real frequency spectrum. However, in non-Hermitian systems, this condition no  
 381 longer holds, allowing complex frequency spectrum to emerge.

382 Despite the presence of non-Hermiticity, Bloch's theorem remains valid for systems that maintain linearity and  
 383 periodicity. Consequently, the dispersion relation is still well-defined, and non-Hermitian systems exhibit frequency  
 384 periodicity in both the real and imaginary axis within the first Brillouin zone. As a result, the frequency spectrum  
 385 under PBC forms closed loops in the complex plane, each characterized by a topological invariant known as the  
 386 winding number, which arises from differential geometry.

387 Under OBC, non-Hermitian systems exhibit the "skin effect", where most eigenmodes localize near the boundaries,  
 388 forming "skin modes" (Yao and Wang, 2018). Studies (Okuma et al., 2020; Yang et al., 2020) show that the existence  
 389 and localization direction of these modes are governed by the winding number: a nonzero winding number indicates  
 390 the presence of skin modes, while its sign determines their localization direction. This relationship establishes a new  
 391 form of bulk-boundary correspondence unique to non-Hermitian physics.

392 In the following section, we outline the method for calculating the winding number of the frequency spectrum  
 393 under PBC, conduct an asymptotic analysis to derive the frequency spectrum under OBC, and extend the non-  
 394 Hermitian bulk-boundary correspondence to Willis media.

#### 395 4.3.1. Winding number of the frequency spectrum under PBC

396 In our system, multiple eigenfrequencies, denoted as  $\omega_\alpha(k)$ , may exist for a given wavenumber under PBC. In  
 397 non-Hermitian systems, the frequency spectrum is generally complex and can form a loop enclosing a base point  $\omega_b$ .

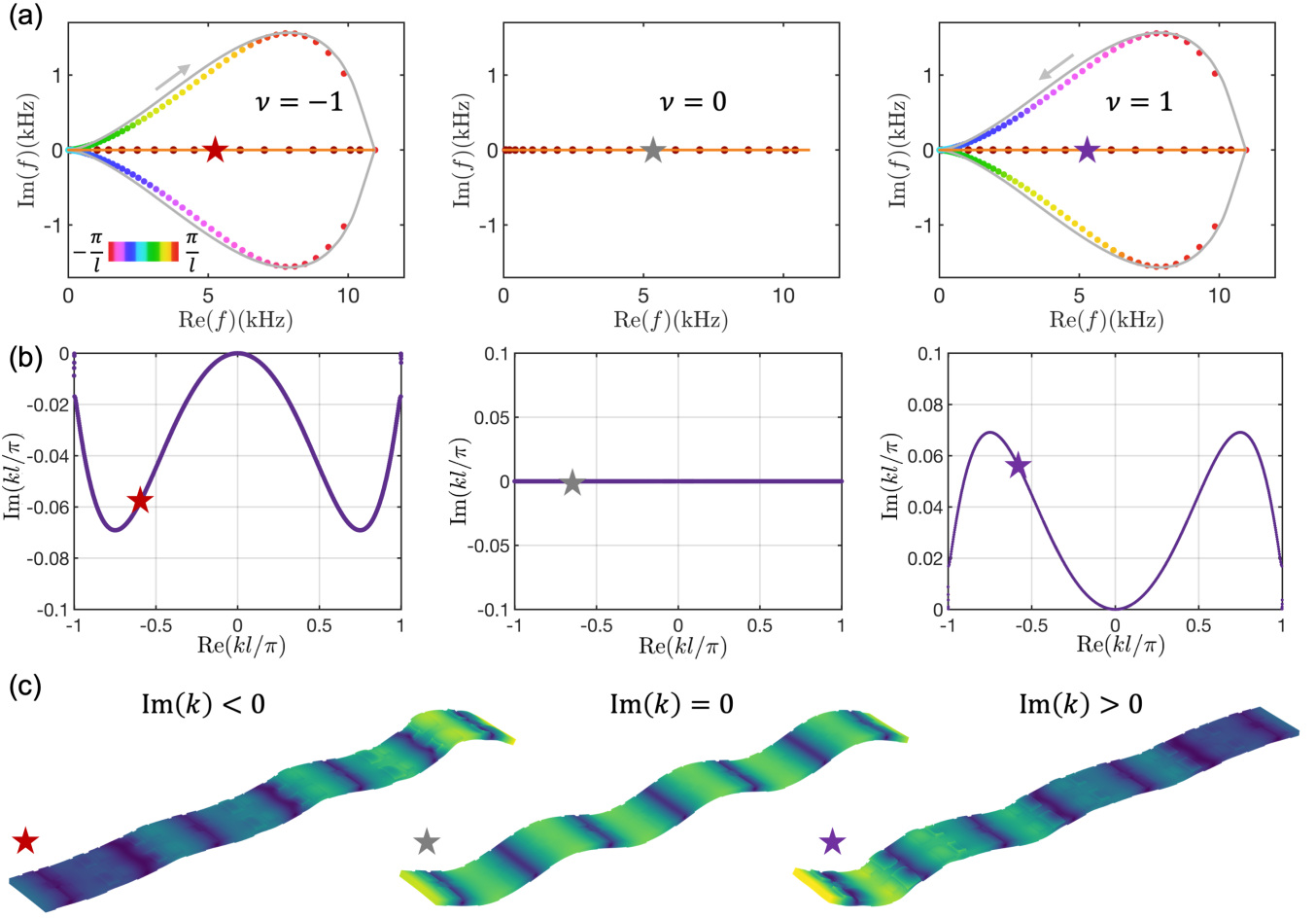


Figure 8: Bulk-boundary correspondence of the winding number and skin mode. (a) Frequency spectrum for the flexural mode of a metabeam under PBC (gradient-colored dots) and fixed boundary conditions (red dots) from COMSOL simulations. The gray solid loop, obtained from the dispersion relation in Eq. (47), and the orange solid line, derived from the BVP in Eq. (78), represent the effective non-Hermitian Willis medium. (b) GBZ associated with the frequency spectrum under fixed boundary conditions, represented by the orange solid line in (a). (c) Eigenmodes from COMSOL simulations corresponding to the starred locations in the frequency spectrum and their associated GBZs. In (a–c), the transfer functions are  $H_1 = -H_2 = 0.3$  in the left panel,  $H_1 = -H_2 = 0$  in the middle panel, and  $H_1 = -H_2 = -0.3$  in the right panel.

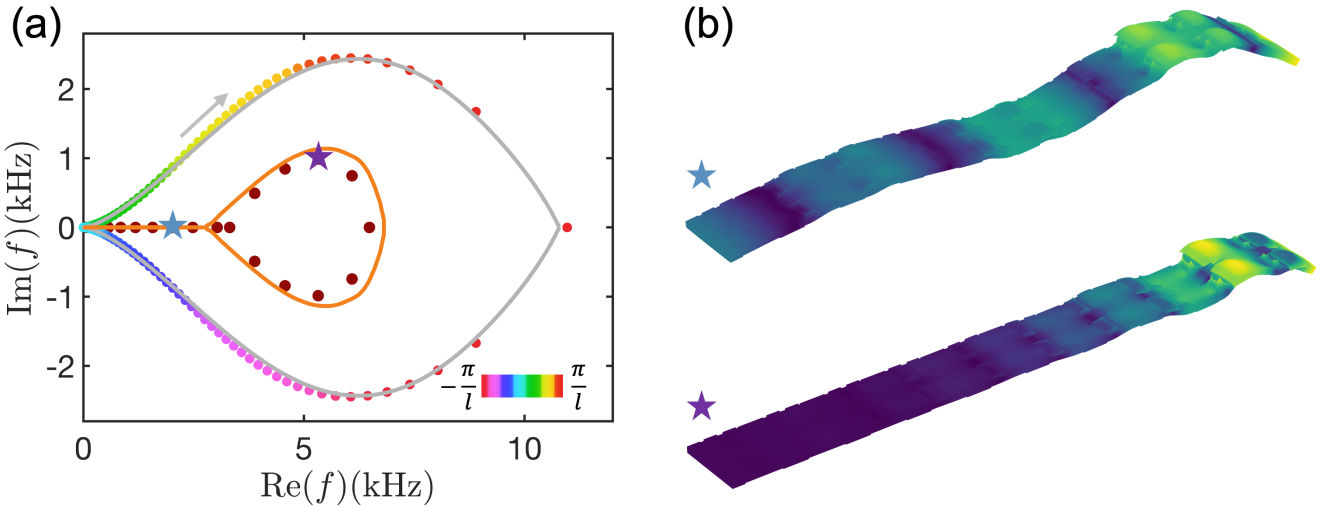


Figure 9: Bulk-boundary correspondence of the winding number and skin mode for transfer functions  $H_1(\omega) = -H_2(\omega) = 1$ . (a) Frequency spectrum for the flexural mode of a metabeam under PBC (gradient-colored dots) and fixed boundary conditions (red dots) from COMSOL simulations. The gray solid loop, obtained from the dispersion relation in Eq. (47), and the orange solid line, derived from the BVP in Eq. (78), represent the effective non-Hermitian Willis medium. (b) Eigenmodes from COMSOL simulations corresponding to the starred locations in the frequency spectrum (a).

398 This loop remains topologically protected as long as  $\omega_b$  remains inside it. In one-dimensional systems, such loops  
 399 are quantitatively characterized by the winding number of the spectrum (Ashida et al., 2020), given by

$$\nu(\omega_b) = \sum_{\alpha} \int_{-\pi/l}^{\pi/l} \frac{dk}{2\pi} \frac{d}{dk} \arg [\omega_{\alpha}(k) - \omega_b]. \quad (69)$$

400 For antisymmetric transfer functions  $H_1(\omega) = -H_2(\omega)$ , the complex frequency spectrum under PBC is shown in  
 401 Fig. 8(a) for  $H_1(\omega) = 0.3$  (left panel),  $H_1(\omega) = 0$  (middle panel), and  $H_1(\omega) = -0.3$  (right panel). In the left panel,  
 402 the spectral loop rotates clockwise as  $k$  varies from  $-\pi/l$  to  $\pi/l$ , yielding a winding number  $\nu(\omega_b) = -1$  for any  
 403 base frequency  $\omega_b$  enclosed by the loop. In the middle panel, the frequency spectrum collapses to a line, indicating  
 404 a winding number of zero for any  $\omega_b$ . In the right panel, the spectral loop rotates counterclockwise as  $k$  varies from  
 405  $-\pi/l$  to  $\pi/l$ , resulting in a winding number  $\nu(\omega_b) = 1$  for any base frequency  $\omega_b$  inside the loop.

406 For antisymmetric transfer functions  $H_1(\omega) = -H_2(\omega) = 1$ , the complex frequency spectrum under PBC is shown  
 407 in Fig. 9(a). The spectrum forms a clockwise loop, indicating a winding number  $\nu(\omega_b) = -1$  for any base frequency  
 408  $\omega_b$  enclosed by the loop. When the antisymmetric transfer function follows Eq. (54), the complex frequency spectrum  
 409 under PBC is shown in Fig. 10(a). In this case, the spectrum consists of a counterclockwise loop on the left and a  
 410 clockwise loop on the right. Consequently, the winding number  $\nu(\omega_b)$  is 1 for any base frequency  $\omega_b$  inside the left  
 411 loop and -1 for any base frequency inside the right loop.

#### 412 4.3.2. Asymptotic analysis of the frequency spectrum under OBC

413 Next, we address the BVP for a finite beam with specified boundary conditions. While non-Hermiticity often  
 414 introduces significant complexity, an intriguing simplification emerges when the beam becomes very long: in this  
 415 limit, the BVP effectively becomes independent of the specific boundary conditions. That is, for  $L \rightarrow \infty$ , certain  
 416 non-Hermitian complexities are mitigated compared to the Hermitian case. In this section, we apply asymptotic  
 417 analysis to determine the frequency spectrum under OBC by taking the beam's length  $L$  to infinity. This approach

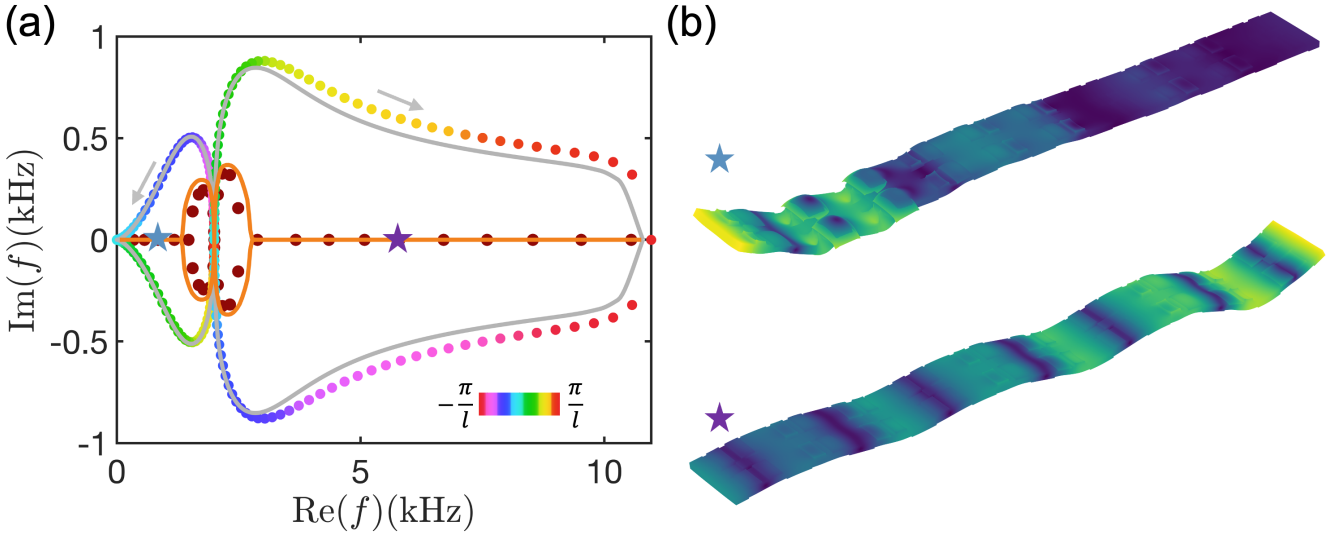


Figure 10: Frequency-dependent skin mode and its bulk-boundary correspondence for transfer functions in Eq. (54). (a) Frequency spectrum for the flexural mode of a metabeam under PBC (gradient-colored dots) and fixed boundary conditions (red dots) from COMSOL simulations. The gray solid loop, obtained from the dispersion relation in Eq. (47), and the orange solid line, derived from the BVP in Eq. (78), represent the effective non-Hermitian Willis medium. (b) Eigenmodes from COMSOL simulations corresponding to the starred locations in the frequency spectrum in (a).

418 yields two algebraic equations whose solutions not only provide the OBC frequency spectrum but also identify the  
 419 GBZ—a concept unique to non-Hermitian systems. All derivations in this section are based on EMT, so the subscript  
 420 eff is omitted for clarity.

421 For the non-Hermitian medium, the dispersion relation in Eq. (47) yields four wavenumber roots for a given  
 422 frequency, denoted as  $k_n$  for  $n = 1, 2, 3, 4$ . The general solution for the transverse displacement of the non-Hermitian  
 423 Willis metabeam is given by

$$w(x) = \sum_{n=1}^4 A_n e^{ik_n x} \quad (70)$$

424 where  $A_n$  are the corresponding coefficients. The rotational angle is expressed as

$$\psi(x) = \sum_{n=1}^4 A_n R_\psi^n e^{ik_n x} \quad (71)$$

425 where  $R_\psi^n$  is defined in Eq. (B.13). Now, we consider the BVP using fixed boundary conditions as an example:

$$w(0) = 0, \quad \psi(0) = 0, \quad w(L) = 0, \quad \psi(L) = 0. \quad (72)$$

426 where  $L$  is the length of the finite metabeam. Substituting the wave solutions into these boundary conditions, we  
 427 obtain the following equations

$$\begin{pmatrix} 1 & 1 & 1 & 1 \\ R_\psi^1 & R_\psi^2 & R_\psi^3 & R_\psi^4 \\ e^{ik_1 L} & e^{ik_2 L} & e^{ik_3 L} & e^{ik_4 L} \\ R_\psi^1 e^{ik_1 L} & R_\psi^2 e^{ik_2 L} & R_\psi^3 e^{ik_3 L} & R_\psi^4 e^{ik_4 L} \end{pmatrix} \begin{pmatrix} A_1 \\ A_2 \\ A_3 \\ A_4 \end{pmatrix} = \begin{pmatrix} 0 \\ 0 \\ 0 \\ 0 \end{pmatrix} \quad (73)$$

428 Setting the determinant of the coefficient matrix to zero yields the frequency spectrum under fixed boundary conditions  
 429

$$\begin{vmatrix} 1 & 1 & 1 & 1 \\ R_\psi^1 & R_\psi^2 & R_\psi^3 & R_\psi^4 \\ e^{ik_1 L} & e^{ik_2 L} & e^{ik_3 L} & e^{ik_4 L} \\ R_\psi^1 e^{ik_1 L} & R_\psi^2 e^{ik_2 L} & R_\psi^3 e^{ik_3 L} & R_\psi^4 e^{ik_4 L} \end{vmatrix} = 0 \quad (74)$$

430 Next, we derive the GBZ by extending the method developed for lattice systems (Yokomizo and Murakami, 2019).  
 431 The solution of Eq. (74) simplifies for large  $L$ , forming the corresponding continuum spectrum. Expanding the  
 432 determinant in Eq. (74), we obtain

$$F_1(\vec{k}, \omega) e^{i(k_1+k_2)L} + F_2(\vec{k}, \omega) e^{i(k_1+k_3)L} + F_3(\vec{k}, \omega) e^{i(k_1+k_4)L} \\ + F_4(\vec{k}, \omega) e^{i(k_2+k_3)L} + F_5(\vec{k}, \omega) e^{i(k_2+k_4)L} + F_6(\vec{k}, \omega) e^{i(k_3+k_4)L} = 0 \quad (75)$$

433 Here,  $\vec{k} = [k_1, k_2, k_3, k_4]$ , and  $F_i(\vec{k}, \omega)$  ( $i = 1, 2, \dots, 6$ ) are coefficients that depend on both frequency and wavenumbers,  
 434 obtained by expanding the determinant in Eq. (74). We now analyze the asymptotic behavior of the solutions  
 435 of Eq. (75) for large  $L$ , where the wavenumbers are ordered as  $\text{Im}(k_1) < \text{Im}(k_2) < \text{Im}(k_3) < \text{Im}(k_4)$  for convenience.

436 If  $\text{Im}(k_2) \neq \text{Im}(k_3)$ , only one leading term proportional to  $F_6(\vec{k}, \omega) e^{i(k_3+k_4)L}$  remains in Eq. (75) in the limit of  
 437 large  $L$ . This leads to

$$F_6(\vec{k}, \omega) = 0 \quad (76)$$

438 which does not depend on  $L$  and does not allow for a continuous frequency spectrum.

439 On the other hand, when  $\text{Im}(k_2) = \text{Im}(k_3)$ , two leading terms proportional to  $e^{i(k_2+k_4)L}$  and  $e^{i(k_3+k_4)L}$  remain,  
 440 allowing Eq. (75) to be rewritten as

$$e^{i(k_2-k_3)L} = -\frac{F_6(\vec{k}, \omega)}{F_5(\vec{k}, \omega)} \quad (77)$$

441 In such a case, we can expect that the difference between  $\text{Re}(k_2)$  and  $\text{Re}(k_3)$  can be changed almost continuously  
 442 for a large  $L$ , producing continuum frequency spectrum.

443 Finally, in the asymptotic limit  $L \rightarrow \infty$ , the boundary value problem of the nonlocal non-Hermitian metabeam  
 444 reduces to two algebraic equations:

$$|\mathbf{H}(\omega, k)| = 0, \\ \text{Im}(k_2(\omega)) = \text{Im}(k_3(\omega)). \quad (78)$$

445 For a given complex frequency  $\omega$ , the first equation in Eq. (78) yields four frequency-dependent wavenumbers  $k_1(\omega)$ ,  
 446  $k_2(\omega)$ ,  $k_3(\omega)$ , and  $k_4(\omega)$ , ordered as  $\text{Im}(k_1) < \text{Im}(k_2) < \text{Im}(k_3) < \text{Im}(k_4)$ . Among these, the second and third  
 447 wavenumbers satisfy the second equation in Eq. (78). The first equation is complex and can be decomposed into two  
 448 real equations, yielding a total of three real equations involving four independent real variables:  $\text{Re}(\omega)$ ,  $\text{Im}(\omega)$ ,  $\text{Re}(k)$ ,  
 449 and  $\text{Im}(k)$ . As a result, the solutions  $(\text{Re}(\omega), \text{Im}(\omega), \text{Re}(k), \text{Im}(k))$  form continuous curves in the four-dimensional  
 450 space. When projected onto the complex  $\omega$ -plane, these solutions appear as continuous curves, ensuring that the  
 451 frequency spectrum remains continuous. Similarly, their projection onto the complex  $k$ -plane forms continuous curves,  
 452 known as the GBZ. The GBZ extends the Brillouin zone concept from Hermitian physics and plays a fundamental

453 role in non-Hermitian physics. It is crucial for reconstructing the bulk-boundary correspondence of the Chern number  
454 and topological edge modes, as well as for computing the Green's function to determine system responses, such as  
455 stress or strain, under external excitations in engineering applications.

456 As mentioned earlier, Eq. (78) includes a complex equation. Unlike in non-Hermitian local media, where dis-  
457 persion relations can be transformed into polynomial equations and efficiently solved using resultant-based methods  
458 from algebraic geometry, the dispersion relations here are transcendental. Consequently, the resultant-based method  
459 fails, necessitating direct numerical solutions. However, solving complex equations numerically is challenging since  
460 many numerical methods are designed for real-valued equations. To address this, for a given variable such as  $\text{Re}(\omega)$ ,  
461 Eq. (78) can be reformulated as three real equations involving three real independent unknowns. Numerical tech-  
462 niques such as Newton's method, iterative solvers, or gradient-based optimization can then be applied. Here, we  
463 use "fsolve" function in MATLAB. By sweeping  $\text{Re}(\omega)$  over the desired range, continuous frequency spectra and  
464 generalized Brillouin zones can be obtained.

465 In deriving Eq. (78), fixed boundary conditions were used. However, in the asymptotic limit, the frequency  
466 spectrum equation in Eq. (78) remains independent of the specific boundary conditions. For other boundary  
467 conditions, such as free, simply supported, or mixed conditions, the coefficients  $F_i(\vec{k}, \omega)$  ( $i = 1, 2, \dots, 6$ ) will change,  
468 but the spectrum condition  $\text{Im}(k_2(\omega)) = \text{Im}(k_3(\omega))$  remains unaffected. Therefore, the frequency spectrum can be  
469 determined by solving Eq. (75) regardless of the boundary conditions. In other words, the frequency spectrum under  
470 OBC is independent of the specific type of boundary conditions.

471 The frequency spectra under OBC for various transfer functions are shown as orange solid lines in Fig. 8(a), Fig.  
472 9(a), and Fig. 10(a), closely matching the eigenfrequencies obtained from COMSOL simulations (red dots). Minor  
473 discrepancies arise due to the finite beam length in the COMSOL model and diminish as the beam length increases.  
474 The corresponding eigenmodes, shown in Fig. 8(c), Fig. 9(b), and Fig. 10(b), exhibit localization at the edges and  
475 are therefore identified as skin modes. These skin modes display exponential localization, with exponential factors  
476 determined by the GBZ. For instance, the GBZ corresponding to the frequency spectrum in Fig. 8(a) is shown in  
477 Fig. 8(b). In the left panel of Fig. 8(b), the GBZ is below the horizontal axis, indicating positive exponential factors,  
478 leading to eigenmodes that grow from left to right, as seen in the left panel of Fig. 8(c). In the middle panel of Fig.  
479 8(b), the GBZ lies on the horizontal axis, signifying zero exponential factors, corresponding to extended eigenmodes,  
480 as shown in the middle panel of Fig. 8(c). In the right panel of Fig. 8(b), the GBZ is above the horizontal axis,  
481 indicating negative exponential factors, resulting in eigenmodes that grow from right to left, as depicted in the right  
482 panel of Fig. 8(c).

#### 483 4.3.3. Bulk-boundary correspondence

484 In the previous sections, we introduced the methods for calculating the winding number and the frequency  
485 spectrum under OBC, along with the concept of skin modes. In this section, we unify these concepts through  
486 bulk-boundary correspondence.

487 Bulk-boundary correspondence has two key aspects. The first concerns the relationship between the frequency  
488 spectra under PBC and OBC, which holds for both EMT and COMSOL simulations. In non-Hermitian systems, the  
489 OBC spectrum is always enclosed by the PBC spectrum. As shown in Fig. 8(a), for small transfer functions, the  
490 OBC spectrum remains real and is encircled by the PBC spectrum. As the transfer function magnitude increases,

491 the OBC spectrum becomes complex while still remaining enclosed by the PBC spectrum, as seen in Fig. 9(a). For  
492 resonant transfer functions in Fig. 10(a), the PBC spectrum splits into two separate loops, each enclosing the OBC  
493 spectrum. These cases illustrate the fundamental relationship between the PBC and OBC spectra, reinforcing the  
494 principles of bulk-boundary correspondence in non-Hermitian systems.

495 The second aspect of bulk-boundary correspondence describes the relationship between the sign of the winding  
496 number at a base frequency (the eigenfrequency of an eigenmode under OBC) and the localization direction of skin  
497 modes. If the winding number at a base frequency is negative, the corresponding skin mode localizes at the right  
498 edge, as shown in the left panels of Fig. 8(a,c). If the winding number is zero, the eigenmode remains extended, as  
499 depicted in the middle panels of Fig. 8(a,c). Conversely, if the winding number is positive, the skin mode localizes at  
500 the left edge, as shown in the right panels of Fig. 8(a,c). These relationships hold for different transfer functions, as  
501 further demonstrated in Fig. 9 and Fig. 10. Instead of computing the GBZ, which is complex and computationally  
502 demanding, bulk-boundary correspondence provides a more efficient way to determine the localization of skin modes.  
503 By simply checking the sign of the winding number from the PBC spectrum, the localization behavior of skin modes  
504 can be directly inferred.

## 505 5. Application

### 506 5.1. Nonreciprocal filtering and amplification

507 In conventional designs, filters and amplifiers are treated as separate components that cannot be directly inte-  
508 grated. However, as shown in the previous section, our system exhibits direction-dependent gain: waves traveling  
509 from left to right are amplified, while those traveling from right to left are attenuated. This nonreciprocal property,  
510 enabled by Willis media, allows filtering and amplification to be seamlessly integrated into a single metabeam.

511 Specifically, for constant antisymmetric transfer functions  $H_1(\omega) = -H_2(\omega) = 0.3$ , the dispersion curves in Fig.  
512 11(c–e) show that waves always decay from left to right but are amplified from right to left. As a result, when a  
513 signal enters from the left, the measured output on the right is attenuated, whereas a signal entering from the right  
514 is amplified on the left. By simply switching the input and detection positions, the metabeam can function either  
515 as a filter or an amplifier. The frequency responses for these two cases are compared in Fig. 11(a), clearly showing  
516 that the right output is attenuated for a left-side input, while the left output is amplified for a right-side input.

517 While conventional frequency-selective filters attenuate signals within a specific passband while leaving out-of-  
518 band signals largely unchanged, many applications require the additional capability to amplify out-of-band signals.  
519 Our Willis metabeam achieves this dual functionality by utilizing antisymmetric local resonant transfer functions (see  
520 Eq. (54)). Specifically, a left-to-right traveling wave is amplified for frequencies below 2 kHz but attenuated above  
521 2 kHz, functioning as a low-stop high-amplifying filter (LSHAF). By reversing the input and output positions, the  
522 system instead operates as a low-amplifying high-stop filter (LAHSF), amplifying low-frequency components while  
523 attenuating higher frequencies. Numerical results for these two modes, shown in Fig. 11(b) and Fig. 11(c), confirm  
524 the expected behaviors of LSHAF and LAHSF. Together, these designs offer a novel approach to frequency-selective  
525 filtering and amplification, surpassing the capabilities of conventional high-pass or bandpass filters.

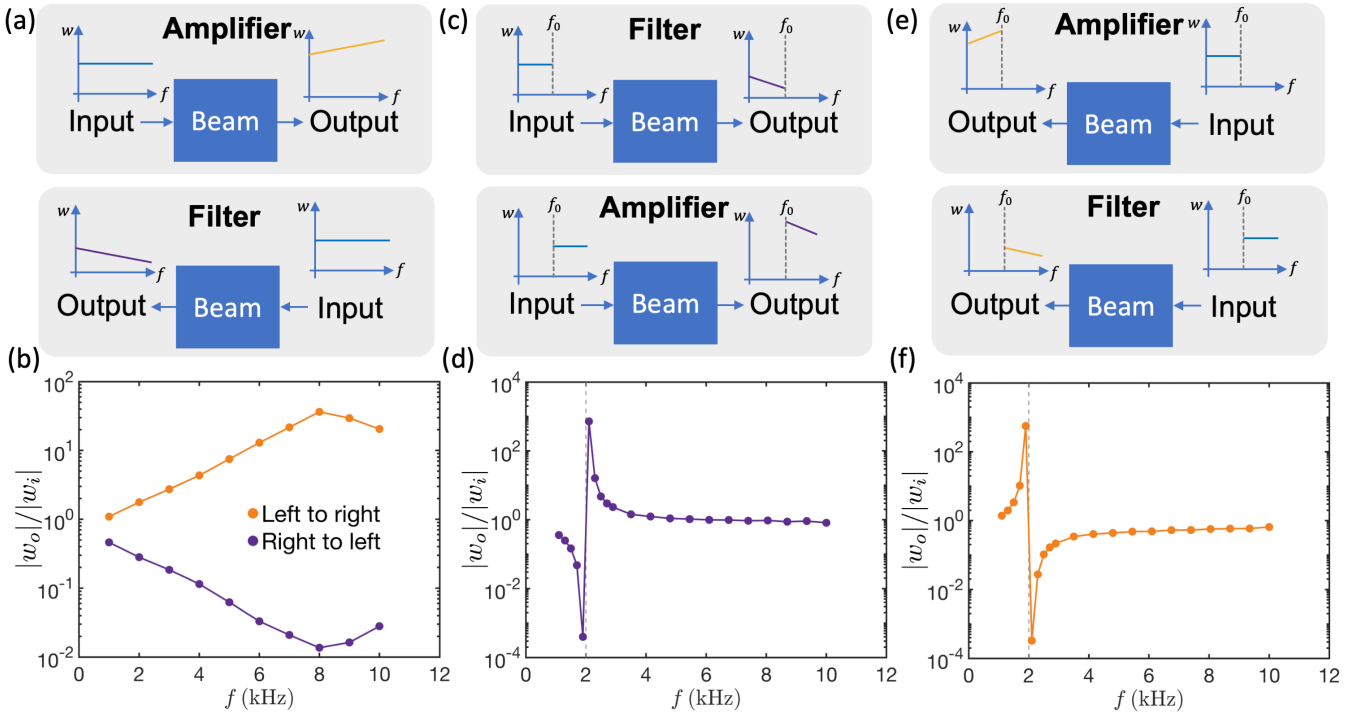


Figure 11: Utilizing nonreciprocal wave behavior for filtering and amplification. (a) For constant antisymmetric transfer functions, the Willis beam amplifies signals propagating from left to right while acting as a filter for signals traveling from right to left. (b) The ratio of output  $w_0$  to input  $w_i$  signal as a function of excitation frequency for (a). (c) For resonant antisymmetric transfer functions, the Willis beam filters out low-frequency signals (below  $f_0$ ) and amplifies high-frequency signals (above  $f_0$ ) when the signal is input from the left and output at the right. (d) The ratio of output  $w_0$  to input  $w_i$  signal as a function of excitation frequency for (c), with the dashed gray line indicating the resonant frequency  $f_0 = 2\text{kHz}$ . (e) For resonant antisymmetric transfer functions, the Willis beam filters out high-frequency signals (above  $f_0$ ) and amplifies low-frequency signals (below  $f_0$ ) when the signal is input from the right and output at the left. (f) The ratio of output  $w_0$  to input  $w_i$  signal as a function of excitation frequency for (e), with the dashed gray line marking the resonant frequency  $f_0 = 2\text{kHz}$ .

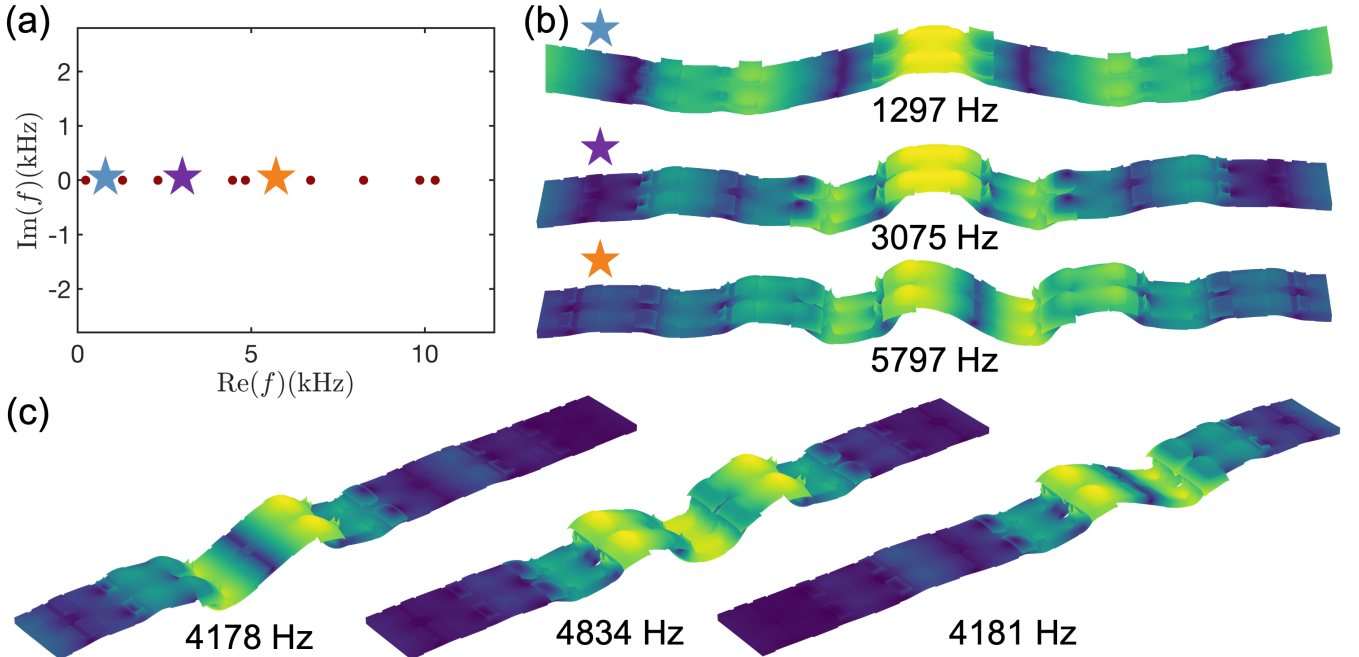


Figure 12: Non-Hermitian interface modes. (a) The frequency spectrum of a finite beam with 10 unit cells, where the interface is located at the 5th and 6th unit cells. The transfer functions for the left five unit cells are  $H_1 = -H_2 = -0.3$ , while for the right five unit cells, they are  $H_1 = -H_2 = 0.3$ . (b) Eigenmodes and their corresponding eigenfrequencies at the starred locations in the frequency spectrum of (a). (c) Eigenmodes and their eigenfrequencies for interfaces located between the 3rd and 4th unit cells (left panel), between the 5th and 6th unit cells (middle panel), and between the 7th and 8th unit cells (right panel).

526    5.1.1. Non-Hermitian interface modes and its potential application in energy harvest

527    In energy harvesting, external energy sources are often distributed across a broad area, while the harvester itself  
528    is confined to a single location. Efficiently channeling energy from multiple source points to the harvester presents  
529    a significant challenge. One approach to address this is through skin modes with a real-valued spectrum, where the  
530    real spectrum ensures system stability and prevents unwanted energy feedback from the sensor-actuator circuit into  
531    the beam. These modes naturally concentrate energy along a boundary, regardless of the source location, allowing  
532    the harvester to be placed there for effective energy collection. However, boundary localization inherently limits  
533    the flexibility of harvester placement. To overcome this constraint, we utilize non-Hermitian interface modes with  
534    a real spectrum to enable energy localization at user-defined interfaces. This approach maintains efficient energy  
535    concentration while significantly expanding the possible locations for harvester installation.

536    In the left and right panels of Fig. 8(c), the localization directions of the two eigenmodes are reversed. By directly  
537    connecting these configurations, each consisting of five unit cells, a beam with ten unit cells is formed, creating an  
538    interface at the center. As a result, the mode shape becomes a localized mode at the interface, as shown in Fig.  
539    12(b). The OBC frequency spectrum remains real and is presented in Fig. 12(a), where all eigenmodes correspond  
540    to interface modes localized at the interface. For instance, three eigenmodes corresponding to the starred points  
541    in Fig. 12(a) are shown in Fig. 12(b), demonstrating that interface modes span a broad frequency range. This  
542    is particularly significant because external energy sources typically operate over a wide range of frequencies. By  
543    adjusting the interface position, energy localization can be achieved at user-defined locations. For example, the  
544    interface mode is localized at the prescribed interface between the 3rd and 4th unit cells in the left panel of Fig.  
545    12(c), between the 5th and 6th unit cells in the middle panel, and between the 7th and 8th unit cells in the right  
546    panel. In conclusion, our design potentially enables efficient energy concentration, allows for a user-defined harvester  
547    position, and supports energy harvesting over a broad frequency range.

548    6. Conclusion

549    We developed an EMT for nonlocal non-Hermitian Willis metabeams, incorporating sensor-actuator interactions  
550    to enable active wave control. Using source-driven homogenization, we derived a dynamic effective medium model  
551    that accurately captures high-frequency and short-wavelength wave behavior, overcoming the limitations of classical  
552    homogenization approaches. This framework integrates non-Hermitian physics and Willis couplings, allowing precise  
553    control over wave amplification, attenuation, and nonreciprocal propagation.

554    Numerical validation through COMSOL simulations confirms the accuracy of our EMT in predicting wave dis-  
555    persions and effective material properties. Additionally, we establish a bulk-boundary correspondence for nonlocal  
556    non-Hermitian Willis media, linking winding numbers to skin modes and extending topological wave mechanics to  
557    elastodynamic systems.

558    Beyond theoretical advancements, we demonstrate applications in nonreciprocal wave control, interface-localized  
559    energy harvesting, and low-frequency shear wave manipulation. These findings lay the foundation for active meta-  
560    materials with tunable wave properties, opening new possibilities in wave-based computing, vibration control, and  
561    energy harvesting.

562 **CRediT authorship contribution statement**

563 Shaoyun Wang: Writing – review & editing, Writing – original draft, Validation, Methodology, Investigation,  
 564 Formal analysis, Conceptualization. Guoliang Huang: Writing – review & editing, Validation, Supervision, Funding  
 565 acquisition, Formal analysis, Conceptualization, Methodology.

566 **Declaration of Competing Interest**

567 The authors declare no known competing financial interests or personal relationships that could have influenced  
 568 the work reported in this paper.

569 **Acknowledgments**

570 The authors thank Dr. Zhanyu Li and Dr. Wen Cheng for their valuable discussions. Guoliang Huang ac-  
 571 knowledges support from the Air Force Office of Scientific Research under Grant Nos. AF 9550-18-1-0342 and AF  
 572 9550-20-1-0279, with Dr. Byung-Lip (Les) Lee as the Program Manager.

573 **Appendix A. Geometric and material parameters**

574 The geometric parameters of the model in Fig. 2(a) are listed in Table A.1. The background beam is made of  
 575 aluminum with a Young's modulus of 70 GPa, a Poisson ratio of 0.33, and a density of 2700 kg/m<sup>3</sup>. The piezoelectric  
 576 patches are composed of PZT-5H, with material properties available in the COMSOL material library. The capacitor  
 577  $C_0$  in Eq. (12) has a value of -0.611 pF.

Table A.1: Geometry parameters of 3D model

Parameter	Value (Unit)	Parameter	Value (Unit)
$w$	21.9 mm	$l$	20 mm
$w_1$	16.1 mm	$l_1$	12 mm
$w_2$	8 mm	$l_2$	4 mm
$w_3$	3.5 mm	$l_3$	2.9 mm
$h_b$	2 mm	$h_p$	0.5 mm

578 **Appendix B. Green's function**

579 *Appendix B.1. Displacement response in Timoshenko beam*

580 Eliminating  $M$ ,  $F$ , and  $\psi$  in the governing equations Eq. (6), we obtain

$$D_0 \frac{\partial^4 w}{\partial x^4} + J_0 \omega^2 \left( 1 + \frac{D_0 P_0}{G_0 J_0} \right) \frac{\partial^2 w}{\partial x^2} + \left( \frac{J_0 \rho_0 \omega^4}{G_0} - \rho_0 \omega^2 \right) w = -\frac{\partial q}{\partial x} + \left( 1 - \frac{J_0}{G_0} \omega^2 \right) f - \frac{D_0}{G_0} \frac{\partial^2 f}{\partial x^2} + D_0 \frac{\partial^2 p}{\partial x^2} + D_0 \frac{\partial^3 s}{\partial x^3} + J_0 \omega^2 \frac{\partial s}{\partial x} \quad (\text{B.1})$$

581 If only shear force is applied as  $f = \delta(x)$ , the equations can be reduced as

$$D_0 \frac{\partial^4 w}{\partial x^4} + J_0 \omega^2 \left( 1 + \frac{D_0 P_0}{G_0 J_0} \right) \frac{\partial^2 w}{\partial x^2} + \left( \frac{J_0 \rho_0 \omega^4}{G_0} - \rho_0 \omega^2 \right) w = \left( 1 - \frac{J_0}{G_0} \omega^2 \right) \delta(x) - \frac{D_0}{G_0} \frac{\partial^2 \delta(x)}{\partial x^2} \quad (\text{B.2})$$

582 The Fourier transform of this equation is

$$w(\omega, k) = \frac{1}{D_0} \frac{1 - \frac{J_0}{G_0} \omega^2 + \frac{D_0}{G_0} k^2}{(k^2 + a^2)(k^2 + b^2)} \quad (\text{B.3})$$

583 Here  $a = ik_1$ ,  $b = k_2$ , and  $k_1$  (pure real) and  $k_2$  (pure real) satisfy the dispersion relation of Timoshenko beam for a  
584 given angular frequency  $\omega$

$$\det[\zeta(k, \omega)] = 0. \quad (\text{B.4})$$

585 The inverse Fourier transform using MATLAB symbolic calculation is

$$w(\omega, x) = -\frac{1}{2D_0} \frac{1 - \frac{J_0}{G_0} \omega^2 - \frac{D_0}{G_0} a^2}{(a^2 - b^2)a} e^{-a|x|} + \frac{1}{2D_0} \frac{1 - \frac{J_0}{G_0} \omega^2 - \frac{D_0}{G_0} b^2}{(a^2 - b^2)b} e^{-b|x|} \quad (\text{B.5})$$

586 or equivalently,

$$w(\omega, x) = \frac{1}{2D_0} \frac{1 - \frac{J_0}{G_0} \omega^2 + \frac{D_0}{G_0} k_1^2}{(k_1^2 + k_2^2)ik_1} e^{-ik_1|x|} - \frac{1}{2D_0} \frac{1 - \frac{J_0}{G_0} \omega^2 - \frac{D_0}{G_0} k_2^2}{(k_1^2 + k_2^2)k_2} e^{-k_2|x|} \quad (\text{B.6})$$

587 Smilarly, for delta source  $q$  only, the displacement response is

$$w(\omega, x) = \frac{1}{2D_0(k_1^2 + k_2^2)} e^{-ik_1|x|} \text{sgn}(x) - \frac{1}{2D_0(k_1^2 + k_2^2)} e^{-k_2|x|} \text{sgn}(x), \quad (\text{B.7})$$

588 for delta source  $p$  only, the displacement response is

$$w(\omega, x) = \frac{ik_1}{2(k_1^2 + k_2^2)} e^{-ik_1|x|} - \frac{k_2}{2(k_1^2 + k_2^2)} e^{-k_2|x|}, \quad (\text{B.8})$$

589 and for delta source  $s$  only, the displacement response is

$$w(\omega, x) = -\frac{-D_0 k_1^2 + J_0 \omega^2}{2D_0(k_1^2 + k_2^2)} e^{-ik_1|x|} \text{sgn}(x) + \frac{D_0 k_2^2 + J_0 \omega^2}{2D_0(k_1^2 + k_2^2)} e^{-k_2|x|} \text{sgn}(x) \quad (\text{B.9})$$

## 590 Appendix B.2. The Green's function

591 Because the system preserves the translational symmetry, applying the linear combination of the four type point  
592 load  $f_0\delta(x - x')$ ,  $q_0\delta(x - x')$ ,  $p_0\delta(x - x')$ , and  $s_0\delta(x - x')$  at  $x'$  simultaneously, the displacement response function  
593 responded at  $x$  is

$$\begin{aligned} w(x', x) &= (p_0 A_1 + s_0 \text{sgn}(x - x') A_2 + f_0 A_3 + q_0 \text{sgn}(x - x') A_4) e^{-ik_1|x-x'|} \\ &\quad + (p_0 A_1 a_1 + s_0 \text{sgn}(x - x') A_2 a_2 + f_0 A_3 a_3 + q_0 \text{sgn}(x - x') A_4 a_4) e^{-k_2|x-x'|} \\ &= \mathbf{B}_1(x - x')^T \mathbf{Q}_0 e^{-ik_1|x-x'|} + \mathbf{B}_2(x - x')^T \mathbf{Q}_0 e^{-k_2|x-x'|} \end{aligned} \quad (\text{B.10})$$

594 where

$$\mathbf{B}_1(x) = \begin{bmatrix} A_1 \\ \text{sgn}(x - x') A_2 \\ A_3 \\ \text{sgn}(x - x') A_4 \end{bmatrix}, \quad \mathbf{B}_2(x) = \begin{bmatrix} A_1 a_1 \\ \text{sign}(x - x') A_2 a_2 \\ A_3 a_3 \\ \text{sign}(x) A_4 a_4 \end{bmatrix}, \quad \mathbf{Q}_0 = \begin{bmatrix} p_0 \\ s_0 \\ f_0 \\ q_0 \end{bmatrix}, \quad (\text{B.11})$$

595 and

$$\begin{aligned}
A_1 &= \frac{ik_1}{2(k_1^2 + k_2^2)}, & a_1 &= -\frac{k_2}{ik_1}, \\
A_2 &= \frac{D_0 k_1^2 - J_0 \omega^2}{2D_0(k_1^2 + k_2^2)}, & a_2 &= \frac{D_0 k_2^2 + J_0 \omega^2}{D_0 k_1^2 - J_0 \omega^2}, \\
A_3 &= \frac{1}{2D_0} \frac{1 - \frac{J_0}{G_0} \omega^2 + \frac{D_0}{G_0} k_1^2}{(k_1^2 + k_2^2) ik_1}, & a_3 &= -\frac{ik_1}{k_2} \frac{1 - \frac{J_0}{G_0} \omega^2 - \frac{D_0}{G_0} k_2^2}{1 - \frac{J_0}{G_0} \omega^2 + \frac{D_0}{G_0} k_1^2}, \\
A_4 &= \frac{1}{2D_0(k_1^2 + k_2^2)}, & a_4 &= -1.
\end{aligned} \tag{B.12}$$

596 Meanwhile, the response functions  $\psi(x', x)$ ,  $F(x', x)$ , and  $M(x', x)$  can be assumed as

$$\begin{aligned}
\psi(x', x) &= R_\psi^1(x - x') \mathbf{B}_1(x - x')^T \mathbf{Q}(x') e^{-ik_1|x-x'|} + R_\psi^2(x - x') \mathbf{B}_2(x - x')^T \mathbf{Q}(x') e^{-k_2|x-x'|} \\
F(x', x) &= R_F^1(x - x') \mathbf{B}_1(x - x')^T \mathbf{T} \mathbf{Q}(x') e^{-ik_1|x-x'|} + R_F^2(x - x') \mathbf{B}_2(x - x')^T \mathbf{T} \mathbf{Q}(x') e^{-k_2|x-x'|} \\
M(x', x) &= R_M^1(x - x') \mathbf{B}_1(x - x')^T \mathbf{Q}(x') e^{-ik_1|x-x'|} + R_M^2(x - x') \mathbf{B}_2(x - x')^T \mathbf{Q}(x') e^{-k_2|x-x'|}
\end{aligned} \tag{B.13}$$

597 Inserting them into the first three equations of Eq. (6) with the aid of Eq. (B.10), we obtain the following linear  
598 equations

$$\begin{aligned}
-\operatorname{sgn}(x - x') ik_1 R_\psi^1(x - x') + \frac{R_M^1(x - x')}{D_0} &= 0 \\
R_\psi^1(x - x') + \frac{R_F^1(x - x')}{G_0} &= -\operatorname{sgn}(x - x') ik_1 \\
-\operatorname{sgn}(x - x') ik_1 R_F^1(x - x') &= -\rho_0 \omega^2
\end{aligned} \tag{B.14}$$

599 for  $R_\psi^1(x - x')$ ,  $R_F^1(x - x')$ ,  $R_M^1(x - x')$ , and the linear equations

$$\begin{aligned}
-\operatorname{sgn}(x - x') k_2 R_\psi^2(x - x') + \frac{R_M^2(x - x')}{D_0} &= 0 \\
R_\psi^2(x - x') + \frac{R_F^2(x - x')}{G_0} &= -\operatorname{sgn}(x - x') k_2 \\
-\operatorname{sgn}(x - x') k_2 R_F^2(x - x') &= -\rho_0 \omega^2
\end{aligned} \tag{B.15}$$

600 for  $R_\psi^2(x - x')$ ,  $R_F^2(x - x')$ ,  $R_M^2(x - x')$ . Solving these equations yields  $R_\psi^1(x - x')$ ,  $R_F^1(x - x')$ ,  $R_M^1(x - x')$ , as well  
601 as  $R_\psi^2(x - x')$ ,  $R_F^2(x - x')$ , and  $R_M^2(x - x')$ .

602 Therefore, the Green's function in the frequency domain is

$$\mathbf{G}(\omega, x - x') = \mathbf{R}_1(x - x') \mathbf{B}_1(x - x')^T e^{-ik_1|x-x'|} + \mathbf{R}_2(x - x') \mathbf{B}_2(x - x')^T e^{-k_2|x-x'|} \tag{B.16}$$

603 and

$$\mathbf{R}_1(x) = \begin{bmatrix} R_M^1(x) \\ R_F^1(x) \\ 1 \\ R_\psi^1(x) \end{bmatrix}, \quad \mathbf{R}_2(x) = \begin{bmatrix} R_M^2(x) \\ R_F^2(x) \\ 1 \\ R_\psi^2(x) \end{bmatrix}. \tag{B.17}$$

604 And the state vector response  $\mathbf{u}(x)$  at  $x$ , excited by a source vector  $\mathbf{Q}(x')$  at  $x'$ , is given by

$$\mathbf{u}(x) = \int \mathbf{G}(\omega, x - x') \mathbf{Q}(x') dx'. \quad (\text{B.18})$$

## 605 Appendix C. Symmetry conditions of Green's function

606 As shown in the middle panel of Fig. 2(b), the periodic actuators can be regarded as periodic scatterers, inducing  
607 multiple scattering effects. To account for these effects, we construct the Green's function of the background beam  
608 and analyze its symmetry. The Green's function for Eq. (6) satisfies

$$\zeta_1 \mathbf{G}(x - x') = \delta(x - x') \mathbf{I} \quad (\text{C.1})$$

609 where the analytical expression of Green's function is presented in [Appendix B](#). Using the Fourier transform

$$G_{ij}(\omega, k) = \frac{1}{\sqrt{2\pi}} \int_{-\infty}^{\infty} G_{ij}(\omega, x - x') e^{ik(x-x')} d(x - x'), \quad i, j = 1, 2, 3, 4. \quad (\text{C.2})$$

610 We find the corresponding Green's function  $\mathbf{G}(\omega, k)$  in the frequency-wavenumber domain satisfies

$$\zeta(\omega, k) \mathbf{G}(\omega, k) = \mathbf{I}. \quad (\text{C.3})$$

611 It is evident that  $\zeta(\omega, k)$  satisfies  $\zeta(\omega, k) = \zeta^\dagger(\omega, k)$ ,  $\zeta(\omega, k) = \zeta^T(\omega, -k)$ , and  $\zeta(\omega, k) = \zeta^*(-\omega, -k)$ . Consequently,  
612 the Green's function  $\mathbf{G}(\omega, k)$  also satisfies the Hermitian condition for given  $\omega$  and  $k$

$$\mathbf{G}(\omega, k) = \mathbf{G}^\dagger(\omega, k), \quad \mathbf{G}(\omega, k) = \mathbf{G}^T(\omega, -k), \quad \mathbf{G}(\omega, k) = \mathbf{G}^*(-\omega, -k) \quad (\text{C.4})$$

613 Using the inverse Fourier transform

$$G_{ij}(\omega, x - x') = \frac{1}{\sqrt{2\pi}} \int_{-\infty}^{\infty} G_{ij}(\omega, k) e^{ik(x-x')} dk, \quad i, j = 1, 2, 3, 4, \quad (\text{C.5})$$

614 the Green's function  $\mathbf{G}(\omega, x - x')$  satisfies the following symmetry

$$\mathbf{G}(\omega, x - x') = \mathbf{G}^\dagger(\omega, x - x'), \quad \mathbf{G}(\omega, x - x') = \mathbf{G}^T(\omega, x' - x), \quad \mathbf{G}(\omega, x - x') = \mathbf{G}^*(-\omega, x' - x) \quad (\text{C.6})$$

## 615 Appendix D. Derivation of effective constitutive relations

616 The  $\zeta$  is not a singular matrix in general, so Eq. (22) can be rewritten as

$$\mathbf{u}_{\text{ext}} = \mathbf{u}_{\text{eff}} + \zeta^{-1} \mathbf{Q}_{\text{eff}}. \quad (\text{D.1})$$

617 In addition, through the elimination of the local source vector  $\mathbf{Q}_0$  in Eq. (23) and Eq. (24), we find

$$\beta \mathbf{u}_{\text{ext}} = (\mathbf{I} - \beta \mathbf{S}) \mathbf{Q}_{\text{eff}} l. \quad (\text{D.2})$$

618 Subtracting Eq. (D.2) by the product of  $\beta$  to Eq. (D.1) gives

$$\beta (\mathbf{u}_{\text{eff}} + \zeta^{-1} \mathbf{Q}_{\text{eff}}) = (\mathbf{I} - \beta \mathbf{S}) \mathbf{Q}_{\text{eff}} l \quad (\text{D.3})$$

619 Reorganizing yields the effective constitutive relations in Eq. (25)

$$\mathbf{Q}_{\text{eff}} = [(\mathbf{I} - \beta \mathbf{S}) l - \beta \zeta^{-1}]^{-1} \beta \mathbf{u}_{\text{eff}} \quad (\text{D.4})$$

620 **Appendix E. Retrieval of local polarizability tensor**

621 Due to the complexity of the unit cell geometry, accurately relating the local polarizability tensor  $\beta$  to the transfer  
622 functions  $H_1(\omega)$  and  $H_2(\omega)$  analytically is challenging. In this section, we employ a retrieval method to numerically  
623 extract the local polarizability tensor, as illustrated in Fig. 3(a). The local state vector  $\mathbf{u}_{\text{loc}}$  is directly obtained from  
624 COMSOL, while the local source vector  $\mathbf{Q}$  is extracted using the scattering method. For each test, given the known  
625  $\mathbf{u}_{\text{loc}}$  and  $\mathbf{Q}$ , we obtain four equations from Eq. (11) with  $\beta$  as the unknown. Since the polarizability tensor contains  
626 16 unknowns, four independent scattering tests are conducted to construct a system of 16 equations, enabling the  
627 unique determination of these unknowns.

628 *Appendix E.1. Numerical extraction of the local source vector*

629 Here, we utilize the extracted displacement field in the frequency domain to inversely determine the local source  
630 vector  $\mathbf{Q}$ . A unit cell is embedded in the middle of the background beam, with perfect matching layers on both  
631 sides (not shown). A unit transverse force is applied at a specified position in the background beam, as illustrated  
632 in Fig. 3(a). In this section, we use asymmetric constant transfer function with  $H_1(\omega) = 0.35$  and  $H_2(\omega) = -0.25$ .  
633 According to Eq. (B.10), the analytical displacement response function at position  $x$  for an excitation applied at the  
634 origin is given by

$$w(0, x) = \mathbf{B}_1(x)^T \mathbf{Q}_0 e^{-ik_1|x|} + \mathbf{B}_2(x)^T \mathbf{Q}_0 e^{-k_2|x|}. \quad (\text{E.1})$$

635 Meanwhile, the scattered displacement field is extracted from COMSOL. For each test, we perform two simulations:  
636 one with the transfer function set to zero and another with a nonzero transfer function. The scattered displacement  
637 field is then obtained by subtracting the displacement field of the zero-transfer-function case from that of the nonzero-  
638 transfer-function case. For the  $i$ th test, we acquire the scattered displacement vector  $\mathbf{w}^i = [w^i(0, x_1), \dots, w^i(0, x_N)]^T$   
639 at positions  $\mathbf{x} = [x_1, x_2, \dots, x_N]^T$ . At each position, Eq. (E.1) must be satisfied, leading to

$$\begin{aligned} & \left[ \mathbf{B}_1(x_1)^T e^{-ik_1|x_1|} + \mathbf{B}_2(x_1)^T e^{-k_2|x_1|} \right] \mathbf{Q}^i = w^i(0, x_1) \\ & \left[ \mathbf{B}_1(x_2)^T e^{-ik_1|x_2|} + \mathbf{B}_2(x_2)^T e^{-k_2|x_2|} \right] \mathbf{Q}^i = w^i(0, x_2) \\ & \quad \dots \\ & \left[ \mathbf{B}_1(x_N)^T e^{-ik_1|x_N|} + \mathbf{B}_2(x_N)^T e^{-k_2|x_N|} \right] \mathbf{Q}^i = w^i(0, x_N). \end{aligned} \quad (\text{E.2})$$

640 Here,  $N$  is chosen to be greater than 4, and  $\mathbf{Q}^i$  is determined using the least squares method. To achieve the desired  
641 precision, a large integer  $N$  (2000 in this study) is selected. By solving the overdetermined system using the least

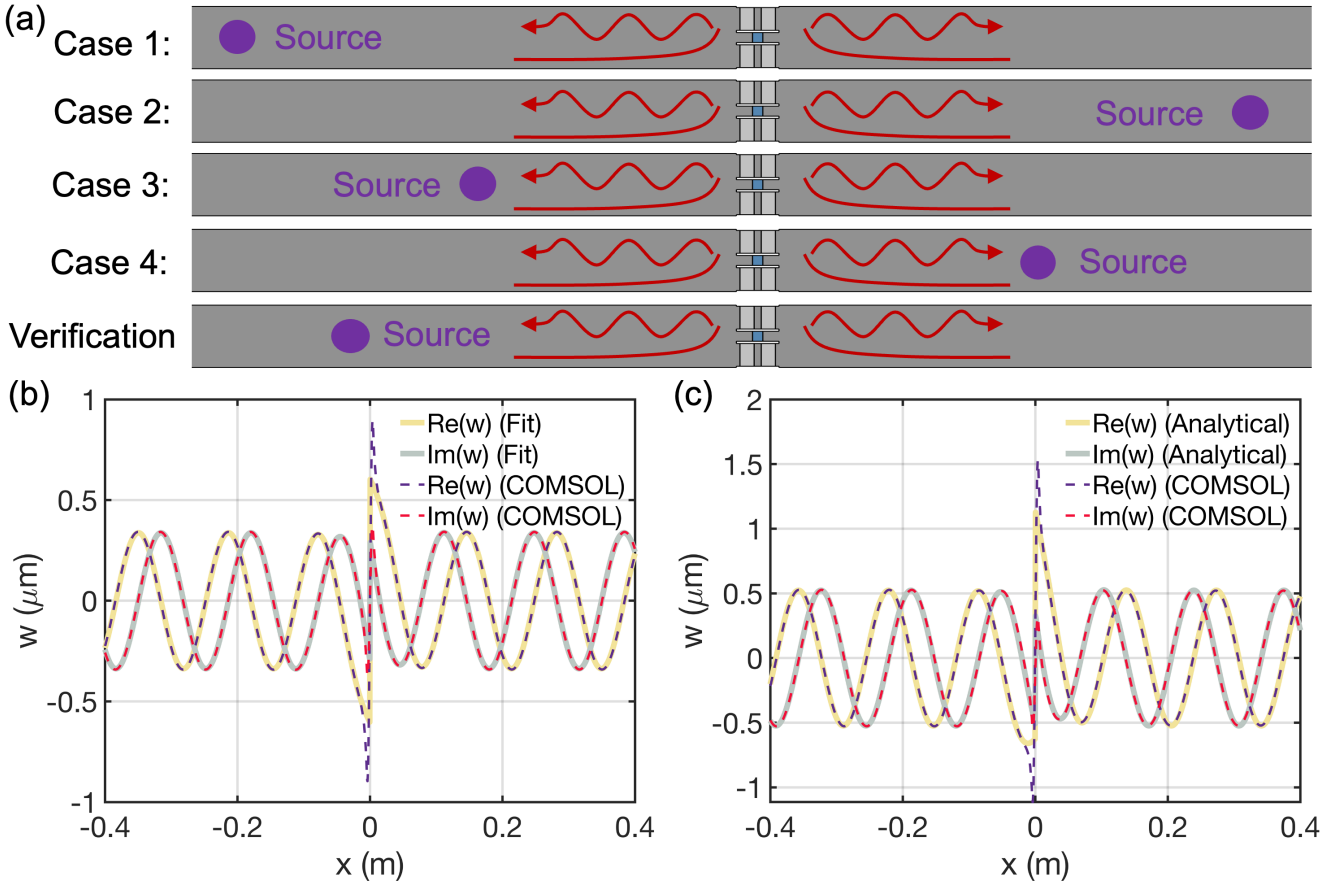


Figure E.13: Numerical extraction of the polarizability tensor. (a) Four numerical tests for extracting the polarizability tensor, along with an additional case for verification. (b) Real part (purple dashed line) and imaginary part (red dashed line) of the scattered displacement field from COMSOL simulations for the first case in (a), compared with the fitted response of a point source (yellow solid line for the real part and gray solid line for the imaginary part). (c) Real part (purple dashed line) and imaginary part (red dashed line) of the scattered displacement field from COMSOL simulations for the verification case in (a), compared with the analytical response of a point source derived from the four tests in (a) (yellow solid line for the real part and gray solid line for the imaginary part).

squares method, we obtain

$$\mathbf{Q}^i = \mathcal{G}^{-1} \mathbf{w}^i \quad (\text{E.3})$$

where  $(\cdot)^{-1}$  denotes the Moore–Penrose pseudoinverse, and the rectangular matrix  $\mathcal{G}$  is defined as

$$\mathcal{G} = \begin{bmatrix} \mathbf{B}_1(x_1)^T e^{-ik_1|x_1|} + \mathbf{B}_2(x_1)^T e^{-ik_2|x_1|} \\ \mathbf{B}_1(x_2)^T e^{-ik_1|x_2|} + \mathbf{B}_2(x_2)^T e^{-ik_2|x_2|} \\ \dots \\ \mathbf{B}_1(x_N)^T e^{-ik_1|x_N|} + \mathbf{B}_2(x_N)^T e^{-ik_2|x_N|} \end{bmatrix} \quad (\text{E.4})$$

To assess the accuracy of the inverse extraction, we compare the analytical scattered displacement field, computed using Eq. (E.1) with the inversely obtained  $\mathbf{Q}^i$ , against the scattered displacement field extracted from the COMSOL simulation for the first case, as shown in Fig. 3(b). The real and imaginary parts of both results closely match, except in the region very close to the unit cell, where microstructural effects become significant. This confirms that the point source assumption is valid for our study and that the inverse extraction method is reliable.

649 Appendix E.2. Numerical extraction of the polarizability tensor

650 Now we have four local source vectors for four tests. The four local state vectors can be extracted in COMOSL  
651 directly. Therefore, for these four tests, the following condition is satisfied according to Eq. (11)

$$\mathbf{Q}^i = \boldsymbol{\beta} \mathbf{u}_{\text{loc}}^i, \quad i = 1, 2, 3, 4, \quad (\text{E.5})$$

652 These linear equations can also be expressed as:

$$\mathbf{Q}^i = u_{\text{loc}}^i(1)\boldsymbol{\beta}_1 + u_{\text{loc}}^i(2)\boldsymbol{\beta}_2 + u_{\text{loc}}^i(3)\boldsymbol{\beta}_3 + u_{\text{loc}}^i(4)\boldsymbol{\beta}_4, \quad i = 1, 2, 3, 4, \quad (\text{E.6})$$

653 where  $\boldsymbol{\beta}_j$  ( $j = 1, 2, 3, 4$ ) is the  $j$ th column vector of the matrix  $\boldsymbol{\beta}$ , and  $u_{\text{loc}}^i(j)$  ( $j = 1, 2, 3, 4$ ) is the  $j$ th element of the  
654 vector  $\mathbf{u}_{\text{loc}}^i$ . Eq. (E.6) can be reformulated as:

$$\begin{bmatrix} \mathbf{Q}^1 \\ \mathbf{Q}^2 \\ \mathbf{Q}^3 \\ \mathbf{Q}^4 \end{bmatrix} = \begin{bmatrix} u_{\text{loc}}^1(1)\mathbf{I} & u_{\text{loc}}^1(2)\mathbf{I} & u_{\text{loc}}^1(3)\mathbf{I} & u_{\text{loc}}^1(4)\mathbf{I} \\ u_{\text{loc}}^2(1)\mathbf{I} & u_{\text{loc}}^2(2)\mathbf{I} & u_{\text{loc}}^2(3)\mathbf{I} & u_{\text{loc}}^2(4)\mathbf{I} \\ u_{\text{loc}}^3(1)\mathbf{I} & u_{\text{loc}}^3(2)\mathbf{I} & u_{\text{loc}}^3(3)\mathbf{I} & u_{\text{loc}}^3(4)\mathbf{I} \\ u_{\text{loc}}^4(1)\mathbf{I} & u_{\text{loc}}^4(2)\mathbf{I} & u_{\text{loc}}^4(3)\mathbf{I} & u_{\text{loc}}^4(4)\mathbf{I} \end{bmatrix} \begin{bmatrix} \boldsymbol{\beta}_1 \\ \boldsymbol{\beta}_2 \\ \boldsymbol{\beta}_3 \\ \boldsymbol{\beta}_4 \end{bmatrix}, \quad (\text{E.7})$$

655 where  $\mathbf{I}$  is the  $4 \times 4$  identity matrix. We concatenate  $\mathbf{Q}^i$  and  $\boldsymbol{\beta}_i$  ( $i = 1, 2, 3, 4$ ) to form larger vectors and assemble  
656  $\mathbf{u}_{\text{loc}}^i$  ( $i = 1, 2, 3, 4$ ) into a matrix

$$\mathbf{Q} = \begin{bmatrix} \mathbf{Q}^1 \\ \mathbf{Q}^2 \\ \mathbf{Q}^3 \\ \mathbf{Q}^4 \end{bmatrix}, \quad \mathbf{u}_{\text{loc}} = \begin{bmatrix} (\mathbf{u}_{\text{loc}}^1)^T \\ (\mathbf{u}_{\text{loc}}^2)^T \\ (\mathbf{u}_{\text{loc}}^3)^T \\ (\mathbf{u}_{\text{loc}}^4)^T \end{bmatrix}, \quad \mathcal{B} = \begin{bmatrix} \boldsymbol{\beta}_1 \\ \boldsymbol{\beta}_2 \\ \boldsymbol{\beta}_3 \\ \boldsymbol{\beta}_4 \end{bmatrix}. \quad (\text{E.8})$$

657 Then Eq. (E.7) can be expressed as

$$\mathbf{Q} = \mathbf{u}_{\text{loc}} \otimes \mathbf{I} \mathcal{B}, \quad (\text{E.9})$$

658 where  $\otimes$  is the Kronecker product. Solving for  $\mathcal{B}$ , we obtain

$$\mathcal{B} = (\mathbf{u}_{\text{loc}} \otimes \mathbf{I})^{-1} \mathbf{Q} \quad (\text{E.10})$$

659 Finally, the local polarizability matrix  $\boldsymbol{\beta}$  is obtained by rearranging the elements of the vector  $\mathcal{B}$ . Since the polar-  
660 izability matrix is generally frequency-dependent, we conduct these four tests at different frequencies and derive the  
661 frequency-dependent polarizability matrix function through curve fitting.

662 Finally, we verify the local polarizability matrix  $\boldsymbol{\beta}$  through a validation test, as shown in the bottom panel of  
663 Fig. 3(a). In this case, the source position differs from those in the four previous cases. First, the local state  
664 vector is extracted, and then the local source vector is determined by multiplying the local state vector by the local  
665 polarizability matrix. Using Eq. (E.1), the analytical scattered displacement field is then computed for the obtained  
666 local source vector. This analytical result is compared with the scattered displacement field extracted from the

667 COMSOL simulation in Fig. 3(c). The consistency between the two results confirms the validity of the point source  
668 assumption and the reliability of the retrieval method for determining the polarizability matrix.

## 669 Appendix F. Interpretation of nonlocal effective parameters

670 According to our effective medium theory, the effective parameters in Eq. (25) depend on both frequency and  
671 wavenumber. However, for freely propagating waves, frequency and wavenumber are not independent but must satisfy  
672 the dispersion relation given in Eq. (47). This implies that the effective parameters are physically meaningful only  
673 at frequencies and wavenumbers that lie on the dispersion curves corresponding to freely traveling waves. This raises  
674 an apparent paradox: whether the effective parameters remain meaningful for arbitrary frequency and wavenumber,  
675 or whether the assumption of independent frequency and wavenumber in the effective parameters requires further  
676 justification.

677 To treat frequency and wavenumber as independent variables, we must consider waves under external excitation.  
678 We begin by introducing a traveling wave excitation of the form

$$\mathbf{Q}_{\text{ext}}(x, t) = \mathbf{Q}_{\text{ext}}(\omega, k)e^{i(kx - \omega t)} \quad (\text{F.1})$$

679 where  $\mathbf{Q}_{\text{ext}}(\omega, k)$  represents the amplitude, which depends on both frequency and wavenumber. The solution to Eq.  
680 (43) can then be expressed as

$$\mathbf{u}_{\text{eff}}(x, t) = \mathbf{u}_{\text{eff}}(\omega, k)e^{i(kx - \omega t)} \quad (\text{F.2})$$

681 where the amplitude vector satisfies

$$\mathbf{u}_{\text{eff}}(\omega, k) = \mathbf{H}(\omega, k)^{-1}\mathbf{Q}_{\text{ext}}(\omega, k). \quad (\text{F.3})$$

682 If the frequency and wavenumber satisfy the dispersion relation,  $\mathbf{H}(\omega, k)$  becomes singular, causing the amplitude vec-  
683 tor to diverge, similar to resonance in vibrational systems. To eliminate this singularity, damping can be introduced  
684 into the system, ensuring that the amplitude vector remains finite. Conversely, if the frequency and wavenumber do  
685 not satisfy the dispersion relation,  $\mathbf{H}(\omega, k)$  remains nonsingular, and the amplitude vector is naturally finite. In this  
686 case, the amplitude vector depends on  $\mathbf{H}(\omega, k)$ , which in turn is determined by the effective parameters, allowing  
687 frequency and wavenumber to be treated as independent variables.

688 Next, we consider a more realistic harmonic excitation of the form

$$\mathbf{Q}_{\text{ext}}(x, t) = \mathbf{Q}_{\text{ext}}(\omega, x)e^{-i\omega t}, \quad (\text{F.4})$$

689 which can be expanded as

$$\mathbf{Q}_{\text{ext}}(x, t) = \frac{e^{-i\omega t}}{\sqrt{2\pi}} \int_{-\infty}^{\infty} \mathbf{Q}_{\text{ext}}(\omega, k)e^{ikx}dk. \quad (\text{F.5})$$

690 For each Fourier component  $\mathbf{Q}_{\text{ext}}(\omega, k)$ , the corresponding response is given by  $\mathbf{u}_{\text{eff}}(\omega, k)$ . Using the principle of  
691 superposition, the total response can be written as

$$\mathbf{u}_{\text{eff}}(t, x) = \frac{e^{-i\omega t}}{\sqrt{2\pi}} \int_{-\infty}^{\infty} \mathbf{H}(\omega, k)^{-1}\mathbf{Q}_{\text{ext}}(\omega, k)e^{ikx}dk. \quad (\text{F.6})$$

692 This result shows that the state vector response depends on the effective parameters for arbitrary frequency and  
693 wavenumber. Therefore, in the context of excitation problems, frequency and wavenumber can be treated as inde-  
694 pendent variables. Furthermore, this approach offers greater flexibility in modulating the effective parameters, as  
695 both frequency and wavenumber can be controlled. For example, a gradient medium with slowly varying properties  
696 can be designed using the WKB approximation to develop an elastic ray theory, enabling novel wave propagation  
697 phenomena ([Wang et al., 2023](#)).

698 **References**

- 699 Agranovich, V. M. and Ginzburg, V. (2013). *Crystal optics with spatial dispersion, and excitons*, volume 42. Springer  
700 Science & Business Media.
- 701 Altman, C. and Suchy, K. (2011). *Reciprocity, spatial mapping and time reversal in electromagnetics*. Springer  
702 Science & Business Media.
- 703 Alù, A. (2011). First-principles homogenization theory for periodic metamaterials. *Physical Review B—Condensed  
704 Matter and Materials Physics*, 84(7):075153.
- 705 Ashida, Y., Gong, Z., and Ueda, M. (2020). Non-hermitian physics. *Advances in Physics*, 69(3):249–435.
- 706 Baz, A. (2024). Why active willis metamaterials? a controllability and observability perspective. *The Journal of the  
707 Acoustical Society of America*, 156(5):3338–3352.
- 708 Bender, C. M. and Boettcher, S. (1998). Real spectra in non-hermitian hamiltonians having p t symmetry. *Physical  
709 review letters*, 80(24):5243.
- 710 Bender, C. M. and Hook, D. W. (2024). Pt-symmetric quantum mechanics. *Reviews of Modern Physics*, 96(4):045002.
- 711 Chen, Y. and Haberman, M. R. (2023). Controlling displacement fields in polar willis solids via gauge transformations.  
712 *Physical Review Letters*, 130(14):147201.
- 713 Chen, Y., Li, X., Hu, G., Haberman, M. R., and Huang, G. (2020). An active mechanical willis meta-layer with  
714 asymmetric polarizabilities. *Nature communications*, 11(1):3681.
- 715 Chen, Y., Li, X., Scheibner, C., Vitelli, V., and Huang, G. (2021). Realization of active metamaterials with odd  
716 micropolar elasticity. *Nature communications*, 12(1):5935.
- 717 Cheng, W. and Hu, G. (2022). Acoustic skin effect with non-reciprocal willis materials. *Applied Physics Letters*,  
718 121(4).
- 719 Christensen, J., Haberman, M. R., Srivastava, A., Huang, G., and Shmuel, G. (2024). Perspective on non-hermitian  
720 elastodynamics. *Applied Physics Letters*, 125(23).
- 721 Galiffi, E., Tirole, R., Yin, S., Li, H., Vezzoli, S., Huidobro, P. A., Silveirinha, M. G., Sapienza, R., Alù, A., and  
722 Pendry, J. B. (2022). Photonics of time-varying media. *Advanced Photonics*, 4(1):014002–014002.

- 723 Goldstein, H., Poole, C., and Safko, J. (2002). *Classical Mechanics*. Addison Wesley.
- 724 Huang, H., Sun, C., and Huang, G. (2009). On the negative effective mass density in acoustic metamaterials.  
725 *International Journal of Engineering Science*, 47(4):610–617.
- 726 Jackson, J. (2012). *Classical Electrodynamics*. Wiley.
- 727 Landau, L., Landau, L., Lifshits, E., Kosevich, A., Lifshitz, E., and Pitaevskii, L. (1986). *Theory of Elasticity: Volume 7*. Course of theoretical physics. Butterworth-Heinemann.
- 728 729 Landau, L., Lifshitz, E., and Sykes, J. (1976). *Mechanics: Volume 1*. Course of theoretical physics. Butterworth-  
730 Heinemann.
- 731 Lee, J.-H., Zhang, Z., and Gu, G. X. (2023). Dynamic homogenization of heterogeneous piezoelectric media: a polariza-  
732 tion approach using infinite-body green's function. *Journal of the Mechanics and Physics of Solids*, 181:105442.
- 733 Li, J., Shen, C., Díaz-Rubio, A., Tretyakov, S. A., and Cummer, S. A. (2018). Systematic design and experimen-  
734 tal demonstration of bianisotropic metasurfaces for scattering-free manipulation of acoustic wavefronts. *Nature  
735 communications*, 9(1):1342.
- 736 Li, Z., Han, P., and Hu, G. (2024). Willis dynamic homogenization method for acoustic metamaterials based on  
737 multiple scattering theory. *Journal of the Mechanics and Physics of Solids*, 189:105692.
- 738 Li, Z., Qu, H., Zhang, H., Liu, X., and Hu, G. (2022). Interfacial wave between acoustic media with willis coupling.  
739 *Wave Motion*, 112:102922.
- 740 Liu, Y., Liang, Z., Zhu, J., Xia, L., Mondain-Monval, O., Brunet, T., Alù, A., and Li, J. (2019). Willis metamaterial  
741 on a structured beam. *Physical Review X*, 9(1):011040.
- 742 Milton, G. W. (2007). New metamaterials with macroscopic behavior outside that of continuum elastodynamics.  
743 *New Journal of Physics*, 9(10):359.
- 744 Milton, G. W., Briane, M., and Willis, J. R. (2006). On cloaking for elasticity and physical equations with a  
745 transformation invariant form. *New journal of physics*, 8(10):248.
- 746 Milton, G. W. and Willis, J. R. (2010). Minimum variational principles for time-harmonic waves in a dissipative  
747 medium and associated variational principles of hashin-shtrikman type. *Proceedings of the Royal Society A:  
748 Mathematical, Physical and Engineering Sciences*, 466(2122):3013–3032.
- 749 Miri, M.-A. and Alu, A. (2019). Exceptional points in optics and photonics. *Science*, 363(6422):eaar7709.
- 750 Muhafra, K., Haberman, M. R., and Shmuel, G. (2023). Discrete one-dimensional models for the electromomentum  
751 coupling. *Physical Review Applied*, 20(1):014042.
- 752 Muhlestein, M. B., Sieck, C. F., Wilson, P. S., and Haberman, M. R. (2017). Experimental evidence of willis coupling  
753 in a one-dimensional effective material element. *Nature communications*, 8(1):15625.

- 754 Nassar, H., He, Q.-C., and Auffray, N. (2015). Willis elastodynamic homogenization theory revisited for periodic  
755 media. *Journal of the Mechanics and Physics of Solids*, 77:158–178.
- 756 Nassar, H., He, Q.-C., and Auffray, N. (2016). On asymptotic elastodynamic homogenization approaches for periodic  
757 media. *Journal of the Mechanics and Physics of Solids*, 88:274–290.
- 758 Nassar, H., Yousefzadeh, B., Fleury, R., Ruzzene, M., Alù, A., Daraio, C., Norris, A. N., Huang, G., and Haberman,  
759 M. R. (2020). Nonreciprocity in acoustic and elastic materials. *Nature Reviews Materials*, 5(9):667–685.
- 760 Nemat-Nasser, S. and Srivastava, A. (2011). Overall dynamic constitutive relations of layered elastic composites.  
761 *Journal of the Mechanics and Physics of Solids*, 59(10):1953–1965.
- 762 Norris, A. N., Shuvalov, A., and Kutsenko, A. (2012). Analytical formulation of three-dimensional dynamic homoge-  
763 nization for periodic elastic systems. *Proceedings of the Royal Society A: Mathematical, Physical and Engineering  
764 Sciences*, 468(2142):1629–1651.
- 765 Okuma, N., Kawabata, K., Shiozaki, K., and Sato, M. (2020). Topological origin of non-hermitian skin effects.  
766 *Physical review letters*, 124(8):086801.
- 767 Pernas-Salomón, R., Haberman, M. R., Norris, A. N., and Shmuel, G. (2021). The electromomentum effect in  
768 piezoelectric willis scatterers. *Wave Motion*, 106:102797.
- 769 Pernas-Salomón, R. and Shmuel, G. (2018). Dynamic homogenization of composite and locally resonant flexural  
770 systems. *Journal of the Mechanics and Physics of Solids*, 119:43–59.
- 771 Pernas-Salomón, R. and Shmuel, G. (2020a). Fundamental principles for generalized willis metamaterials. *Physical  
772 Review Applied*, 14(6):064005.
- 773 Pernas-Salomón, R. and Shmuel, G. (2020b). Symmetry breaking creates electro-momentum coupling in piezoelectric  
774 metamaterials. *Journal of the Mechanics and Physics of Solids*, 134:103770.
- 775 Ponge, M.-F., Poncelet, O., and Torrent, D. (2017). Dynamic homogenization theory for nonlocal acoustic metama-  
776 terials. *Extreme Mechanics Letters*, 12:71–76.
- 777 Qu, H., Liu, X., and Hu, G. (2022). Mass-spring model of elastic media with customizable willis coupling. *Internation-  
778 al Journal of Mechanical Sciences*, 224:107325.
- 779 Rabczuk, T., Ren, H., and Zhuang, X. (2023). Computational methods based on peridynamics and nonlocal operators.  
780 In *Computational Methods in Engineering & the Sciences*. Springer.
- 781 Sakurai, J. and Napolitano, J. (2017). *Modern Quantum Mechanics*. Cambridge University Press.
- 782 Shokri, B. and Rukhadze, A. A. (2019). *Electrodynamics of Conducting Dispersive Media*. Springer.
- 783 Shore, R. A. and Yaghjian, A. D. (2007). Traveling waves on two-and three-dimensional periodic arrays of lossless  
784 scatterers. *Radio Science*, 42(06):1–40.

- 785 Shuvalov, A., Kutsenko, A., Norris, A., and Poncelet, O. (2011). Effective willis constitutive equations for periodically  
786 stratified anisotropic elastic media. *Proceedings of the Royal Society A: Mathematical, Physical and Engineering*  
787 *Sciences*, 467(2130):1749–1769.
- 788 Sieck, C. F., Alù, A., and Haberman, M. R. (2017). Origins of willis coupling and acoustic bianisotropy in acoustic  
789 metamaterials through source-driven homogenization. *Physical Review B*, 96(10):104303.
- 790 Srivastava, A. (2015). Elastic metamaterials and dynamic homogenization: a review. *International Journal of Smart*  
791 *and Nano Materials*, 6(1):41–60.
- 792 Wang, S., Hu, Z., Wu, Q., Chen, H., Prodan, E., Zhu, R., and Huang, G. (2023). Smart patterning for topological  
793 pumping of elastic surface waves. *Science Advances*, 9(30):eadh4310.
- 794 Wang, S., Shao, N., Chen, H., Chen, J., Qian, H., Wu, Q., Duan, H., Alu, A., and Huang, G. (2025). Temporal  
795 refraction and reflection in modulated mechanical metabeams: theory and physical observation. *arXiv preprint*  
796 *arXiv:2501.09989*.
- 797 Wang, Y., Wu, Q., Tian, Y., and Huang, G. (2024). Non-hermitian wave dynamics of odd plates: Microstructure  
798 design and theoretical modelling. *Journal of the Mechanics and Physics of Solids*, 182:105462.
- 799 Willis, J. R. (1981). Variational principles for dynamic problems for inhomogeneous elastic media. *Wave Motion*,  
800 3(1):1–11.
- 801 Willis, J. R. (1997). Dynamics of composites. In *Continuum micromechanics*, pages 265–290. Springer.
- 802 Willis, J. R. (2009). Exact effective relations for dynamics of a laminated body. *Mechanics of Materials*, 41(4):385–  
803 393.
- 804 Willis, J. R. (2011). Effective constitutive relations for waves in composites and metamaterials. *Proceedings of the*  
805 *Royal Society A: Mathematical, Physical and Engineering Sciences*, 467(2131):1865–1879.
- 806 Willis, J. R. (2012). The construction of effective relations for waves in a composite. *Comptes rendus. Mécanique*,  
807 340(4-5):181–192.
- 808 Wu, Q., Wang, S., Qian, H., Wang, Y., and Huang, G. (2024). Understanding of topological mode and skin mode  
809 morphing in 1d and 2d non-hermitian resonance-based meta-lattices. *Journal of the Mechanics and Physics of*  
810 *Solids*, 193:105907.
- 811 Wu, Q., Xu, X., Qian, H., Wang, S., Zhu, R., Yan, Z., Ma, H., Chen, Y., and Huang, G. (2023). Active metamaterials  
812 for realizing odd mass density. *Proceedings of the National Academy of Sciences*, 120(21):e2209829120.
- 813 Wu, Q., Zhang, X., Shivashankar, P., Chen, Y., and Huang, G. (2022). Independent flexural wave frequency  
814 conversion by a linear active metalayer. *Physical Review Letters*, 128(24):244301.
- 815 Xia, Y., Riva, E., Rosa, M. I., Cazzulani, G., Erturk, A., Braghin, F., and Ruzzene, M. (2021). Experimental  
816 observation of temporal pumping in electromechanical waveguides. *Physical Review Letters*, 126(9):095501.

- 817 Yang, Z., Zhang, K., Fang, C., and Hu, J. (2020). Non-hermitian bulk-boundary correspondence and auxiliary  
818 generalized brillouin zone theory. *Physical Review Letters*, 125(22):226402.
- 819 Yao, S. and Wang, Z. (2018). Edge states and topological invariants of non-hermitian systems. *Physical review  
820 letters*, 121(8):086803.
- 821 Yao, W., Zhong, W., and Lim, C. W. (2009). *Symplectic elasticity*. World Scientific.
- 822 Yokomizo, K. and Murakami, S. (2019). Non-bloch band theory of non-hermitian systems. *Physical review letters*,  
823 123(6):066404.
- 824 Yves, S., Fleury, R., Shmuel, G., Fruchart, M., Vitelli, V., Haberman, M. R., and Alù, A. (2024). Symmetry-driven  
825 phononic metamaterials. *arXiv preprint arXiv:2411.18556*.
- 826 Zhai, Y., Kwon, H.-S., and Popa, B.-I. (2019). Active willis metamaterials for ultracompact nonreciprocal linear  
827 acoustic devices. *Physical Review B*, 99(22):220301.
- 828 Zhang, K., Yang, Z., and Fang, C. (2020). Correspondence between winding numbers and skin modes in non-hermitian  
829 systems. *Physical Review Letters*, 125(12):126402.
- 830 Zhu, R., Liu, X., Hu, G., Sun, C., and Huang, G. (2014). Negative refraction of elastic waves at the deep-  
831 subwavelength scale in a single-phase metamaterial. *Nature communications*, 5(1):5510.